Lignin-derived bimetallic platinum group metal-free oxygen reduction reaction electrocatalysts for acid and alkaline fuel cells

Mohsin Muhyuddin[a], Ariel Friedman[b], Federico Poli[c], Elisabetta Petri[c], Hilah Honig[b], Francesco Basile[d], Andrea Fasolini[d], Roberto Lorenzi[a], Enrico Berretti[e], Marco Bellini[e], Alessandro Lavacchi[e], Lior Elbaz[b], Carlo Santoro[a], Francesca Soavi[c**]*

[a] Department of Materials Science, University of Milano-Bicocca, Via Roberto Cozzi 55, Building U5, 20125, Milan, Italy

[b] Department of Chemistry and the Institute of Nanotechnology and Advanced Materials, Bar-Ilan University, Ramat-Gan, 5290002, Israel

[c] Department of Chemistry "Giacomo Ciamician", CIRI - FRAME, C3 Center for Chemical Catalysis, Alma Mater Studiorum - Università di Bologna, Italy

[d] Department of Industrial Chemistry "Toso Montanari", C3 Center for Chemical Catalysis, Alma Mater Studiorum - Università di Bologna, Italy

[e] Istituto di Chimica Dei Composti OrganoMetallici (ICCOM), Consiglio Nazionale Delle Ricerche (CNR), Via Madonna Del Piano 10, Sesto Fiorentino, 50019, Firenze, Italy

* Corresponding author. ** Corresponding author. carlo.santoro@unimib.it (C. Santoro), francesca.soavi@unibo.it (F. Soavi).

Abstract

Metal-nitrogen-carbons (M-N-Cs) as a reliable substitution for platinum-group-metals (PGMs) for oxygen reduction reaction (ORR) are emerging candidates to rationalize the technology of fuel cells. The development of M-N-Cs can further be economized by consuming waste biomass as an inexpensive carbon source for the electrocatalyst support. Herein, we report the simple fabrication and in-depth characterization of electrocatalysts using lignin-derived activated char. The activated char (LAC) was functionalized with metal phthalocyanine (FePc and MnPc) via atmosphere-controlled pyrolysis to produce monometallic M-N-Cs (L_Mn and L_Fe) and bimetallic M1-M2-N-Cs (L_FeMn) electrocatalysts. Raman spectroscopy and transmission electron microscopy (TEM) revealed a defect-rich architecture. XPS confirmed the coexistence of various nitrogen-containing active moieties. L_Fe and L_FeMn demonstrated appreciable ORR in both acidic and alkaline conditions whereas L_FeMn helped in restricting the peroxide yield, particularly in alkaline media. L_Fe and L_FeMn demonstrated remarkable onset potential (E_{onset}) of ~0.942 V (vs RHE) with an

$E_{1/2}$ of 0.874 V (vs RHE) in 0.1 M KOH. In acid, L_FeMn had an E_{onset} of 0.817 V (vs RHE) and an $E_{1/2}$ of ~0.76 V (vs RHE). Finally, the L_FeMn as a cathode electrocatalyst was integrated and tested in PEMFC and AEMFC. AEMFC demonstrated optimistic performance with a peak power density of 261 mW cm^{-2} at the current density of ~577 mA cm^{-2}.

Keywords

Lignin-derived char; Oxygen reduction reaction; Platinum group metal-free; Proton exchange membrane fuel cell; Anion exchange membrane fuel cell

1. Introduction

Low-temperature fuel cells (FCs) being capable of converting chemical energy into electrical energy without contributing to planetary carbon footprints are one of the most paramount candidates to sustainably address the global energy crises. Within the paradigm of advanced FCs, analogous technologies of proton exchange membrane FCs (PEMFCs) and anion-exchange-membrane FCs (AEMFCs) are capturing scientific attention owing to their unique merits. Both technologies with different pH of electrolytic media realize the incessant translation of energy through hydrogen oxidation reaction (HOR) at the anode and the oxygen reduction reaction (ORR) at the cathode, leaving water as a green byproduct. However, even though FCs are having considerable commercial success, the complex and lethargic ORR constitutes the key hindrance in their practical deployment on a large scale since it is several orders of magnitude slower than the HOR [[1], [2], [3]]. Reduction of oxygen follows multielectron transfer routes with sluggish kinetics, imposing much higher overpotential and thus restricting the overall device efficiency. It is known in the scientific community that ORR usually proceeds either in a bi-electronic or tetra-electronic fashion producing peroxide or water, respectively [[4], [5], [6], [7], [8]]. From the perspective of FCs, the tetra-electronic pathway is essentially important whereas the production of highly reactive peroxide during bi-electronic ORR not only makes the system less energy efficient but also severely affects the integrity of membrane electrode assembly (MEA) and stack architecture. To deal with the aforementioned challenges, platinum group metals (PGMs) are typically employed which eventually make the application of FCs economically impracticable. The use of scarce and expensive Pt in the fabrication of ORR electrocatalysts accounts for more than 55% of the total cost of an FC stack [9,10]. Moreover, state-of-the-art Pt-based electrocatalysts are also notorious for their undesired dissolution, nanoparticle coalescence and poisoning with common contaminants which in turn gravely diminish the electrocatalytic efficiency [10,11]. Therefore, it is an urgent need of the hour to cope with such complications either by reducing the Pt content or by substituting with PGM-free electrocatalysts. In

the pursuit of PGM-free electrocatalysis, metal-nitrogen-carbons (M-N-Cs, M = Mn, Fe, Co, Ni etc.) are emerging as a reliable competitor in which earth-abundant transition metals (TM) having coordination with different nitrogen species (MN_x) make active moieties for ORR within the porous carbonaceous framework [6,[12], [13], [14], [15], [16], [17]].

In the search for an efficacious M-N-C electrocatalyst, various designing parameters must be considered. First comes the porous nature of carbonaceous architecture. Carbon provides a conducive platform for the whole electrochemical activity whereas a high surface area and mesoporous environment boost the mass transport of gaseous reagents to the active sites [18]. Where the intrinsic defects, ruptured facets and structural discontinuities in carbon facilitate the binding of oxygen [19], the dangling bonds present in the unsaturated vacancies also contribute to the doping of secondary elements i.e. nitrogen to generate the active moieties [20]. Furthermore, nitrogen doping breaks the electro-neutrality of the carbon triggering the chemisorption of O_2 [21] and due to enhanced Lewis basicity, pyridinic-nitrogen effectively participates in ORR by subsequently reducing the peroxide intermediate into water [22,23]. Over and above that, the selection of the transition metal is a strategic task in electrocatalyst development as the electrons transfer from metal to oxygen is primarily dictated by the redox potential of the central metal [16,[24], [25], [26]] and hence the plurality of redox sites is one of the foremost prerequisites for O_2 activation and the subsequent reduction [16]. MN_x (x = 2,3,4) is undoubtedly the most electrocatalytically active site in which a central TM atom has coordination with pyridinic nitrogen ligands on the distorted carbon surface and aptly bio-mimic the natural enzyme to reduce oxygen [[27], [28], [29], [30]]. In addition to the conventional exploitation of metal salts and organic precursors of nitrogen and carbon for the fabrication of M-N-Cs, the use of metal macrocyclic compounds i.e. metal phthalocyanine (MPc) and porphyrins have the preferred MN_4 sites. However, a thermomechanical treatment known as pyrolysis becomes inevitably imperative to achieve the mandatory durability and robustness. This occurs by integrating the MN_x active sites onto the carbon backbone, favored by the high-temperature treatment. Although such active sites can be generated using MPc of different first-row TM, $Fe–N_4$ finds its place at the apex of the volcano curve due to its moderate adsorption portfolio [13,16,24,25,31]. It is noteworthy that FePc and MnPc promote the tetra-electronic ORR by rupturing the O–O bond due to the preferable *'d character'*. On the other hand, it was shown that CoPc, NiPc and CuPc tend to catalyze the ORR in a bi-electronic manner, underlined by the high intermediate production [16,24,31,32].

Notwithstanding the fact that Fe–N–Cs are glossing in the arena of PGM-free electrocatalysis, their performance is still inferior compared to PGM-based electrocatalysts, spurring extensive global ventures to understand and improve the activity of Fe–N–Cs [[33], [34], [35], [36], [37], [38], [39]]. To mitigate the efficiency pitfalls, the introduction of a second TM could be useful [40]. Serov et al.

analyzed the influence of Fe interaction with a second TM by developing a series of electrocatalysts using a sacrificial support method (SSM) and observed a substantial upturn in ORR activity after the addition of a second TM [41]. At the present, some acknowledgeable efforts have been made to co-doped Fe and Co [[42], [43], [44], [45], [46]]. However, again the usage of Co challenges the economic rationalization of FCs since it is listed among critical raw materials [47,48] and also Co holds the tendency of producing higher peroxide [17,49]. Moreover, as compared to Co, the supplementation of Mn into Fe-carrying M-N-Cs clearly improves the electrocatalytic activity by keeping the peroxide generation relatively lower which ultimately hastens up the cathodic performance [[50], [51], [52]].

In parallel, a growing scientific interest has recently been witnessed in the development of ORR electrocatalysts using waste biomasses [[53], [54], [55], [56], [57], [58], [59]] and plastics [[60], [61], [62], [63], [64]] as a cheaper and readily available source of carbon and such initiatives could circularly ensure ecological safety. Global agricultural waste generation is gigantically increasing on annual basis [65] and hence, its transformation into innovative materials is rationally justified considering the environmental gains of waste reduction [53]. As already mentioned, porosity and high surface area are primarily required for providing accessibility to the active sites, biomasses owing to trimodal structures efficiently fulfill this prerequisite and act as a tailorable pattern for novel materials fabrication [55,66]. Among these biomass wastes, lignin derived from waste biomass is one of the most produced agricultural wastes. According to an estimation, annual global harvesting of biomass accounts for more than 170 billion metric tons [67] out of which lignin is present up to 25% [68] whereas the pulp and paper industry generates up to 50–70 million tons per year [69,70] which is expected to surpass the figure of 225 million tons annually by the year 2030 [70,71].

Herein, within the core of the circular economy, we valorize real waste lignin and transform it through pyrolysis and activation processes into high surface area char that is then functionalized with mono- and bi-metallic phthalocyanine and tested as PGM-free electrocatalyst for oxygen reduction reaction in acid and alkaline media. After a complete physio-chemical and electrochemical characterization, the lignin-derived PGM-free electrocatalysts are integrated into cathode electrodes and tested in PEMFC and AEMFC.

2. Materials and methods

2.1. Lignin derived activated char (LAC)

Lignin-derived activated char (LAC) was produced by adapting the process reported in Ref. [59]. The raw lignin, a real solid waste of an anaerobic biodigester plant located in Bologna (Biotec Sys srl),

was washed with a water/ethanol mixture and then dispersed in an aqueous solution with a mild activating agent, $KHCO_3$ for 24 h (1:2 of Lignin:$KHCO_3$ in ratio). The dried mold was kept in two identical grids, placed in a tubular oven (ELITE TSH16/50/610-2216E) and pyrolyzed under N_2 flux by heating from room temperature to 850 °C and held for 1 h while keeping the heating and then left to cool down. The biochar resulting from the two grids was mixed and sieved before proceeding with a deashing with 3 M HCl for 8 h and washing with deionized water under a vacuum. In the end, soxhlet extraction with water was performed. The produced LAC featured a specific surface area of 1367 $m^2\ g^{-1}$.

2.2. Electrocatalyst synthesis

The synthesis of electrocatalysts was carried out by functionalizing LAC with the metal(s)-phthalocyanine (MPc) of interest. To begin with, 80 wt.% of LAC was thoroughly mixed with 20 wt.% MPc. Table 1 demonstrates the weight proportions of LAC and MPc set to fabricate monometallic and bimetallic samples. The homogenized mixture obtained in the first step was then transferred into a clean ceramic boat and subjected to a controlled atmosphere tube furnace (Carbolite) for high-temperature pyrolysis. During the pyrolysis, the material was taken from room temperature to 600 °C and held there for 1 h while keeping the heating and cooling ramp rates at 5 °C min^{-1}. Whereas the whole process was performed in 5 wt.% H_2 balanced with N_2 at 100 $cm^3\ min^{-1}$. Afterward, the obtained electrocatalyst was rigorously homogenized by giving a round of ball milling (E_{MAX}, Retsch Gmbh, Germany) at 400 rpm for 40 min using zirconia balls of 3 mm diameter.

Sample Names	LAC (Wt. %)	FePc (Wt. %)	MnPc (Wt. %)
LAC	100	–	–
L_Fe	80	20	–
L_Mn	80	–	20

Sample Names	LAC (Wt. %)	FePc (Wt. %)	MnPc (Wt. %)
L_FeMn	80	10	10

Table 1. Description of the samples studied.

2.3. Structural and morphological characterization

The textural properties of the LAC were evaluated by nitrogen adsorption porosimetry measurements that were carried out at 77 K with an ASAP 2020 system (Micromeritics) after a drying step for 24 h at 413 K. The Brunauer-Emmett-Teller (BET) and density functional (DFT) theories were used to analyze N_2 adsorption isotherm, in order to obtain specific surface area (S_{BET}) and pores size distribution (PSD), respectively.

Thermogravimetry analysis (TGA) was conducted using TA Instrument TGA Q50 analyzer in the oxygen atmosphere, in order to evaluate the ash content of the LAC produced. The analysis was performed by applying a temperature ramp of 10 °C/min from room temperature to 850 °C.

Energy-dispersive X-ray fluorescence (XRF) having an X-ray tube with a molybdenum anode (Bruker Artax 200 spectrometer) was utilized to perform qualitative elemental analysis. For the crystal structure evaluation, X-ray diffraction (XRD, Rigaku Miniflex 600) with a copper source was employed in the 2θ range of 10–90°. To investigate the carbonaceous structure of as-developed electrocatalysts, Raman spectroscopy (LabRam, Jobin Yvon, France) was utilized where helium-neon laser (λ = 632.8 nm) as an excitation source was focused on the sample with the help of BX40 microscope (Olympus, Japan) while a silicon-based CCD system (Sincerity, Jobin Yvon, France) was used to collect the signals.

X-ray photoelectron spectroscopy (XPS) was carried out using a Nexsa spectrometer (England) equipped with a monochromatic, micro-focused, lower Al Ka X-ray (photon energy 1486.6 eV). Survey and high-resolution spectra were acquired at pass energy of 200 eV and 50 eV, respectively. The source power was normally 72 W. All elements' binding energies were recalibrated by setting the CC/CH component of the adventitious carbon 1st peak at 285 eV. The measurements were carried out under UHV conditions, at a base pressure of 5×10^{-10} torr (and no higher than 3×10^{-9} torr). Data analysis was performed using AVANTAGE software. Linear background subtraction was used for all spectra. High-Resolution Transmission electron microscopy (HRTEM) measurements were done using, JEOL JEM 2100, LaB6 filament, 200 kV.

2.4. Electrochemical analysis

The kinetic parameters of the developed electrocatalysts were investigated through the rotating ring disk electrode (RRDE) methodology (Pine Wave Vortex RDE connected with a Pine bipotentiostat). For the preparation of inks, 5 mg of the synthesized electrocatalyst was suspended in a solution containing 985 μL of isopropanol (Alfa Aesar) and 15 μL of 5 wt% Nafion® D-520 (Alfa Aesar). The inks were homogenized by probe sonication for 10 min followed by ultrasonic bath sonication for the next 30 min at ambient temperature. E6R2 series RRDE electrode was used to fabricate the working electrode with 0.2 mg cm^{-2} and 0.6 mg cm^{-2} loadings of each electrocatalyst. In-house prepared 0.5 M H_2SO_4 and 0.1 M KOH solutions were used as the electrolytic media in O_2-saturated circumstances to simulate ORR activity in acidic and alkaline conditions, respectively. The experiments were run in a three-electrode configuration encompassing a Pt-based counter electrode, saturated calomel electrode (SCE) as a reference and RRDE working electrode while 85% IR compensations were made using SP-100 Biologic® potentiostat. In this study, all the potentials are presented with respect to reversible hydrogen potential (RHE) after adding a factor of 0.241 + pH x 0.0591 into the measured potentials which were originally referenced to SCE. Linear sweep voltammetry (LSV) was executed to acquire polarization curves at 5 mV s^{-1} between 1200 and 0 mV vs RHE while maintaining the ring potential ~1200 mV vs RHE. ORR measurements were performed by rotating the RRDE at 1600 rpm. Before getting the actual LSV curves, the electrocatalyst was conditioned with multiple cyclic voltammograms until a stable current was achieved. The peroxide yield and number of electron transfers (n) during ORR were estimated by monitoring the disk current (I_{disk}) and ring current (I_{ring}) using the following equations:(1)Peroxide(%)=200×IringNIdisk+IringN(2)n=4IdiskIdisk+IringN

The electrochemical stability was analyzed by applying 5000 cycles in the potential range between 1100 and 300 mV vs RHE at 50 mV s^{-1} in the O_2-saturated electrolytes by rotating the RRDE (with 0.6 mg cm^{-2} electrocatalyst loading) at 1600 rpm. For making a comparison, ORR polarization curves were obtained again at 5 mV s^{-1}.

2.5. Fuel cell fabrication and testing

2.5.1. AEMFC

All AEMFC electrodes used in this work were prepared as described in detail in our previous publications [72,73]. In brief, the electrocatalyst powder (80 wt.%) was mixed with the ETFE-based anion exchange ionomer powder (20 wt.%) containing benzyl trimethylammonium (BTMA) functional groups in 10 mL of distilled water and 2 propyl alcohol (1:1) solution. The resulting ink was homogenized by 30 min of ultrasound treatment (45 kHz, 100 W) and then sprayed using an

Iwata® spray gun onto the gas diffusion layer TGP-H-60 carbon paper 10% PTFE purchased by Alfa Aesar. The catalyst spray was suspended every once in a while to dry the electrode for 10 s on an 80 °C hot plate and subsequently weighed to control the electrocatalyst correct loading. The anode loading was ca. 0.4 mg_{PtRu} cm^{-2}, the cathode coating was 0.8 $mg_{electrocatalyst}$ cm^{-2}.

The anion exchange membrane (AEM) preparation procedure has previously been described in Ref. [74] and consists of a 10 μM HDPE sheet functionalized with vinylbenzyl chloride monomer by electron-beam radiation grafting (100 kGy absorbed dose). The membrane was subjected to amination treatment with aqueous TMA (45 wt.%). The AEM and the electrodes were immersed in 1 M KOH aqueous solution for 1 h before assembly into a 5 cm^2 fuel cell fixture (Scribner Associates) using a 5 N m torque. The AEMFC was tested with a Scribner Associates 850e fuel cell test station setting the cell temperature at 60 °C. The anode was fed with pure hydrogen at 54 °C (75% relative humidity) at 0.3 L min^{-1} flow rate and the cathode was fed with pure oxygen at 60 °C (100% relative humidity) at 0.6 L min^{-1}. The cell was characterized by consecutive 20 scan voltage experiments from OCV to 0.3 V applying a 10 mV s^{-1} linear sweep.

2.5.2. PEMFC

The electrocatalyst (L_FeMn) was also tested in a PEM-FC. 152 mg of Nafion solution (D1021), 0.566 mL of isopropanol and 0.477 mL of water were added to 26 mg of the electrocatalyst. The ink was sonicated for 1.5 h in ice. The electrocatalyst was sprayed on the Sigracet 29BC gas diffusion layer (GDL) using the airbrush. The final loading was ~4.4 mg cm^{-2}. A commercial gas diffusion electrode (GDE) (Fuel Cells Etc., CST-GDE-01) of 0.2 mg cm^{-2} of pt Pt/C was used at the anode side. The anode GDE was hot pressed with NR-211 Nafion membrane (130 °C) for 5 min. Then, the cathode GDE was assembled without hot pressing the MEA. The cell was tightened up to 10 Nm.

The cell was operated at 80 °C. For testing the MEA, hydrogen (0.5 L min^{-1}) and air (0.7 L min^{-1}) were used at the anode and cathode sides, respectively (both at 80 °C). Break-in was performed by holding the cell at 0.15 mA cm^{-2} until the cell voltage was stabilized (~5 min). Then, the voltage was scanned between 0.0 and 0.7 V (0.025 A/point, 30 s) and from 0.7 V to 0.2 V (0.05 A/point, 30 s).

3. Results and discussion

3.1. Initial characterization of lignin derived activated char

Black char was formed after the pyrolysis of the waste lignin. Importantly, initial screening evaluating the BET surface area (S_{BET}) and the ash content was conducted.

The evaluation of the surface area and pore size distribution was carried out by analyzing the N_2 adsorption/desorption isotherms at 77 K which is reported in Fig. 1a. At low pressures, the isotherm branch of the LAC sample illustrated sharp adsorption inflection which is indicative of type I and materials containing micropores. However, at higher relative pressures of $0.45 < P/P_0 < 1.0$, the presence of an H4 hysteresis loop indicates that LAC is a complex material containing interconnected micropores and mesopores (type IV).

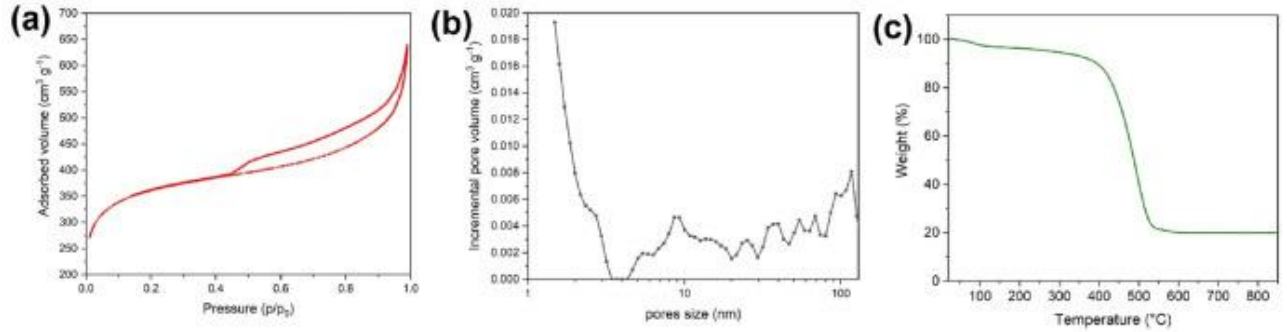

Fig. 1. N_2 adsorption-desorption isotherms (a), pore size distribution (b) and thermogravimetric analysis (c) of LAC.

These observations are confirmed by the DFT pore size distribution that is reported in terms of incremental pore volume in Fig. 1b. The micropore volume (V_{micro}), mesopore volume (V_{meso}) and total pore volume (V_{total}) of the sample are charted in Table 2 along with the BET surface area (S_{BET}). The S_{BET} is 1367 ± 1 $m^2\ g^{-1}$. Such high value is mainly related to micropores and small mesopores (<3 nm). Indeed, V_{micro} (0.40 $cm^3\ g^{-1}$) accounts for the 70% V_{total} (0.57 $cm^3\ g^{-1}$). Larger pores are almost equally distributed from 3 nm up to more than 100 nm, and contribute with only the 20% to V_{total} (V_{meso} = 0.12 $cm^3\ g^{-1}$).

Sample	***V*$_{micro}$ (<2 nm) cm^3 g^{-1}**	***V*$_{meso}$ (2–50 nm) cm^3 g^{-1}**	***V*$_{total}$ cm^3 g^{-1}**	***S*$_{BET}$ m^2 g^{-1}**	**Ash content (%)**
LAC	0.40	0.12	0.57 (<137 nm)	1367 ± 1	19

Table 2. DFT micropore volume (V_{micro}), mesopore volume (V_{meso}) and total pore volume (V_{total}), BET-specific surface area (S_{BET}) and ash content of LAC.

Finally, Fig. 1c reports the thermogravimetric analysis of the LAC produced. The ash content evaluated is reported in Table 2 and is about 19%. This result may depend on the natural origin of the raw material.

3.2. Structural and morphological investigations

Soon after the functionalization of the LAC with the MPc of interest, qualitative elemental analysis was carried out using XRF (Fig. S1**)**. Each sample showed clear peaks of the metal of interest i.e. Fe and/or Mn, justifying the effectiveness of the synthesis process. However, pristine LAC (Fig. S1a) contained a few traces of Fe, Cu and Ni, which probably were present in the raw material or got introduced as contamination during the processing and therefore were minutely present in every sample. Since the relative presence of impurities was too low they were not considered contributors to ORR and were unheeded. Moreover, XRD was employed with the aim of phase identification and two broader peaks that emerged nearly at 25° and 43.5° were indexed to (002) and (101) planes of carbon, respectively, portending the distorted nature of the graphitic matrix [75,76] (Fig. 2a). Only, sample L_Mn demonstrated very tiny peaks of MnO at ~34.9°, ~40.5° and ~58°, consistent with JPDS# 01-089-4835. Kumar et al. also experienced such tiny MnO peaks in the XRD pattern of bimetallic ORR electrocatalysts fabricated by dual functionalization of carbon nanotubes with FePc and MnPc [40]. However, quite interestingly, L_Fe and L_FeMn demonstrated only the diffraction peaks of carbon, giving an impression of the homogenized distribution of Fe and Mn-based species in the carbon matrix without forming coarser crystalline nanoparticles [[76], [77], [78], [79]]. In our case, the usage of MPc in a relatively smaller proportion might have restricted the excessive coalescence of metallic species into coarser nanoparticles. Moreover, appreciable prevention of metal nanoclustering up to a pyrolysis temperature of 600 °C has already been witnessed [80]. The carbonaceous structure of the resultant electrocatalysts was further examined by the way of Raman spectroscopy as demonstrated in Fig. 2b. All the samples revealed typical G (nearly at 1590 cm^{-1}) and D (nearly at 1330 cm^{-1}) bands, due to in-plane stretching of the sp^2 carbon atom with E_{2g} symmetry and breathing mode of A_{1g} symmetry, respectively [81,82]. LAC and L_Mn also exhibited a D′ band in the vicinity of 1613 cm^{-1}. The G band is conventionally ascribed to graphitization content while the D and D’ band emerge because of the structural disruption and induced defects in the original lattice [[81], [82], [83], [84], [85]]. It is worth mentioning that every sample had a higher D peak indicating a greater extent of disorders and defects in the carbon architecture, which could substantially participate in enhancing the ORR activity due to modified electronic and chemical characteristics of the disrupted carbons [76,86,87]. As it is well known, the

ratio of D to G band intensity (I_D/I_G) manifests the degree of disorder in carbon-based materials. I_D/I_G remained always higher than unity where this intensity ratio reached the maximum value of 1.27 for L_Fe followed by 1.18 for L_FeMn which indicates the occurrence of a very high defect density.

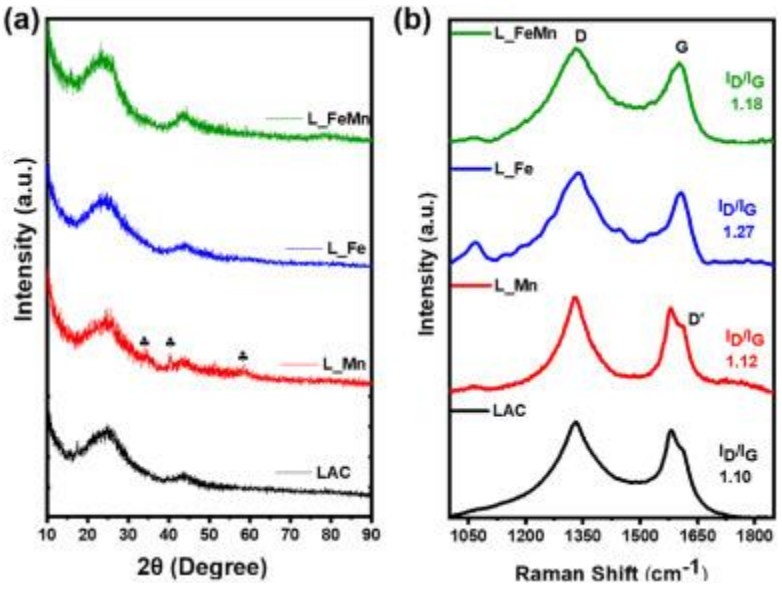

Fig. 2. XRD patterns (a) and Raman spectra (b) of the as-developed samples.

3.3. Surface chemistry and morphology

It was shown that the surface chemistry of the electrocatalysts plays a crucial role in the electrocatalytic activity and the mechanisms that are taking place [88,89]. Therefore, XPS was used to identify the surface composition. The acquired full survey scans provided in Fig. S2 indicate the prevalence of carbon, nitrogen and oxygen as major constituents where silicon is present as an impurity element. In the metal functionalized samples i.e. L_Mn, L_Fe and L_FeMn tiny peaks belonging to Mn and/or Fe can be appreciated while the high-resolution 2p spectra of Mn and Fe in the corresponding samples are additionally displayed in Fig. S3. The intensities of both Mn2p and Fe2p spectra came out to be very low and thus agreed with the XRD findings, suggesting the homogenous presence of metallic content in traces. Li and coworkers also experienced such kind of structure while developing trace bimetallic ORR electrocatalysts [51]. Table S1 summarizes the elemental composition as well as the relative proportion of the nitrogen-based species present in the samples.

As afore discussed in detail, nitrogen is an important ingredient of M-N-Cs and helps in specifying the route of ORR, N 1s high-resolution spectra of the derived samples (Fig. 3) were thoroughly analyzed. Deconvolution of N 1s peak of LAC indicated the occurrence of various nitrogen species such as imine N, pyridinic N, hydrogenated N, graphitic/protonated N, and NO_x, emerging in the

vicinity of their typical binding energies [21,[90], [91], [92], [93], [94], [95]]. Interestingly the metal functionalized sample also demonstrated the presence of M-N_x. Whereas pyridinic N (0.5 at.%) was maximum in LAC with a total nitrogen content of 1.87 at.%. Nitrogen came out to be the highest in L_Fe (3.4 at.%) with the predominance of M-N_x, hydrogenated N–H and graphitic N whereas pyridinic N remained 0.36–38 at.% in all three metal functionalized samples. It is worth mentioning that the co-occurrence of various active sites can be advantageous since each of them performs particular tasks during ORR [52]. Generally, pyridinic N is considered essential for completing the electro-reduction of oxygen, especially as a secondary active site [21]. However, Okada et al. also experienced superior activity of graphitic N owing to lower defect density [96]. Lai et al. experienced the dependency of limiting current density on graphitic N while pyridine N predicted the onset potential [97]. On the other hand, Kabir et al. revealed that hydrogenated N (including pyrrolic and Pyridinic N–H) not only uplifts the reaction kinetics but also acts as key active sites for the 2 + 2 e−transfer mechanism ORR in both alkaline and acidic media while pyridinic N being secondary active site can be helpful in further reducing the peroxide in the alkaline environment [94]. In addition to metal-free nitrogen-based moieties, M-N_x is expected to carry out the direct tetra-electronic reduction of oxygen into water [98]. Moreover, the reactivity of such active sites is also governed by the nature of the electrolyte to which they are exposed and their roles alter as the pH of the electrolyte changes [35]. Shifting from acidic to alkaline conditions switches pyridinic N–H to deprotonated pyridinic N^- which is a preferential adsorption site for O_2 due to enhanced Lewis basicity [35,99].

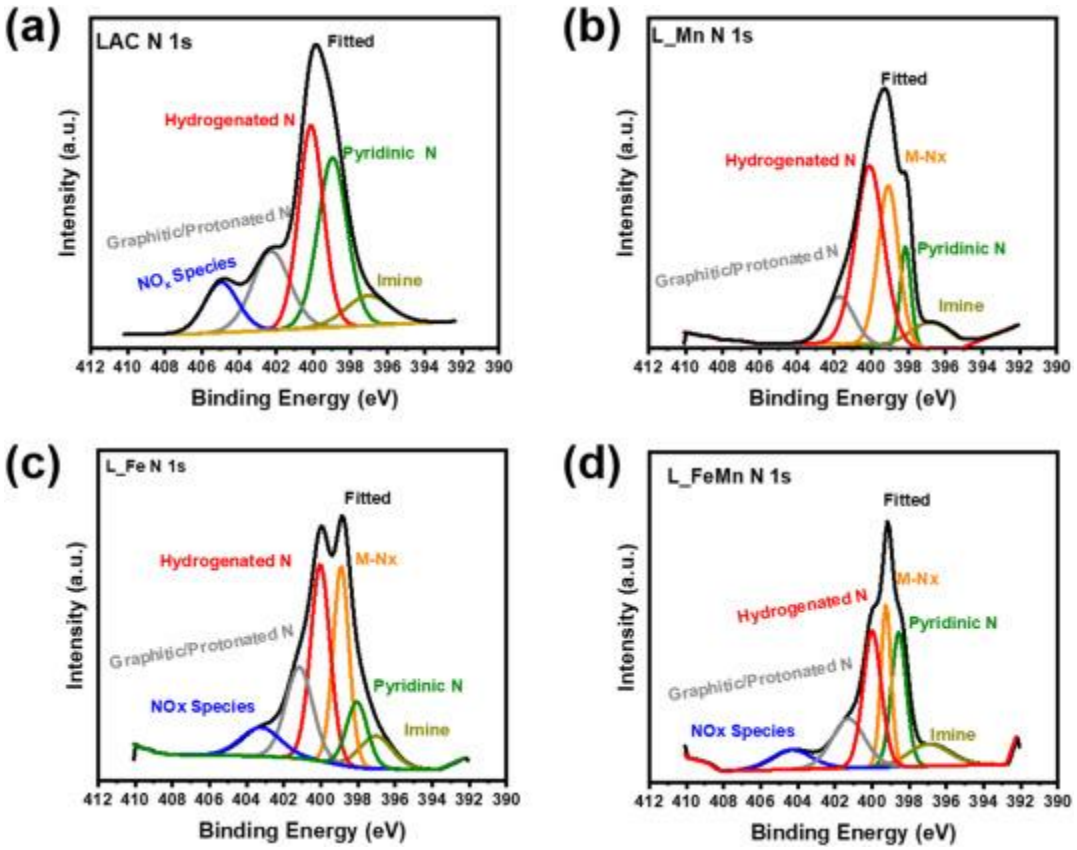

Fig. 3. XPS high-resolution N 1s spectra of the as-developed samples.

The morphological features of the derived samples were studied by the means of TEM. Obtained micrographs are illustrated in Fig. 4. LAC demonstrated a well-developed porous structure. Such aspects of the microstructure were sustained in the MPc functionalized samples as well. Microstructural features could be relatable to the outcomes of Raman spectroscopy and XRD that highlighted the presence of structural defects and disorders. In a high-resolution image of L_Fe (Fig. 4f) a few broken graphitic domains could be appreciated. Interestingly, TEM micrographs of functionalized electrocatalysts didn't show substantial agglomeration or nanoparticle formation of metallic species which further validates the impression of atomically dispersed metallic moieties in a homogenous fashion [100]. EDS presented in Fig. S4 further confirms the elements of interest i.e. Fe and Mn in the corresponding samples whereas peaks of Cu belong to the TEM sample holder and Si is an impurity artifact.

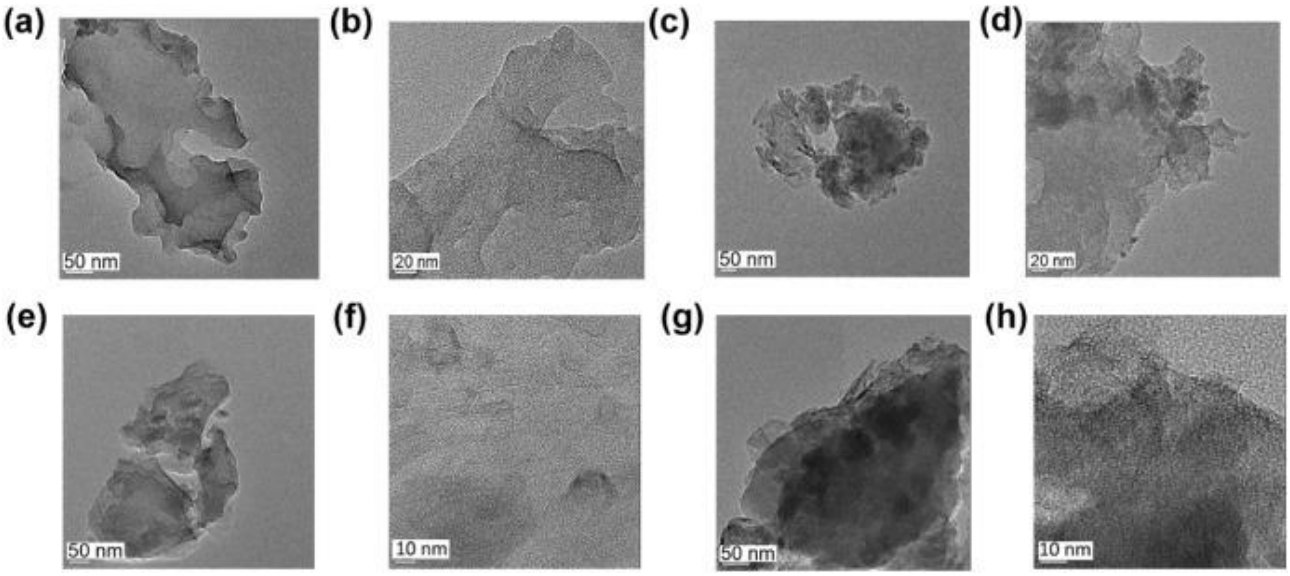

Fig. 4. TEM images of LAC (a, b), L_Mn (c, d), L_Fe (e, f) and L_FeMn (g, h).

3.4. Electrochemical activity

To elucidate the electrocatalytic aptitude of the developed electrocatalysts, RRDE measurements were carried out. Changing the nature of working electrolytes not only modifies the reaction mechanism but different active sites respond to ORR activity differently [101,102]. For that reason, ORR measurements were obtained in alkaline and acidic media, to ensure the utility of the developed electrocatalyst for AEMFC and PEMFCs, respectively. Onset potential (E_{onset}), half-wave potential ($E_{1/2}$) and limiting current density (I_{limit}) are the common performance indicator acquired from RRDE while the electrocatalyst loading on the disk of RRDE may affect the peroxide formation. Therefore,

two different loadings of 0.2 mg cm^{-2} and 0.6 mg cm^{-2} were individually utilized to analyze the electrochemical aspects of the studied electrocatalysts.

3.4.1. ORR performance in alkaline media

Fig. 5 demonstrates the ORR activity in O_2-saturated 0.1 M KOH with electrocatalysts loading of 0.6 mg cm^{-2} while the performance with one-third loading is additionally presented in Supplementary Fig. S5. Polarization curves attained at a 5 mV s^{-1} scan rate highlighted the active nature of the developed electrocatalysts, however, the pristine LAC came out to be the least efficient with a higher overpotential. Remarkably, the functionalization of LAC with MPc categorically improved the kinetics. Among all the counterparts, L_Fe and L_FeMn exhibited the highest E_{onset} of ~0.94 V (vs RHE) with an outstanding $E_{1/2}$ of 0.87 V (vs RHE). I_{limit} remained maximum for L_FeMn. LAC and L_Mn showed $E_{1/2}$ of ~0.75 V (vs RHE) and 0.85 V (vs RHE) respectively, with 0.6 mg cm^{-2} catalyst loadings. Peroxide production showed interesting trends where the electrocatalyst loading also contributed to diminishing the yield of unwanted OH_2^-. A threefold increment in the electrocatalyst loading resulted in a slight positive shift of the $E_{1/2}$ along with a subsequent drop in the peroxide yield. Actually, with higher loading, the produced peroxide gets scavenged and then reduced within the denser layer of the electrocatalyst [[103], [104], [105], [106]]. LAC and L_Mn initially came out to be peroxide-producing electrocatalysts at lower overpotential however a definite decline in the peroxide production can be seen as the applied potential increases. This speculation endorses the probability of a 2 + 2 electrons reduction pathway where the generated peroxide is afterward reduced at the secondary sites. On the other hand, L_Fe and L_FeMn tended to restrict the peroxide formation in a nearly tetra-electronic fashion. In the case of L_FeMn, peroxide yield remained confined to a maximum of ~16% and 8.7% while the electron transfer number was above 3.68 and 3.83 with 0.2 and 0.6 mg cm^{-2} loading, respectively. Overall superior electrocatalytic activity is essentially credited to the dual-doping of Fe and Mn due to which electro-reduction of oxygen was synergistically boosted [40,[50], [51], [52]].

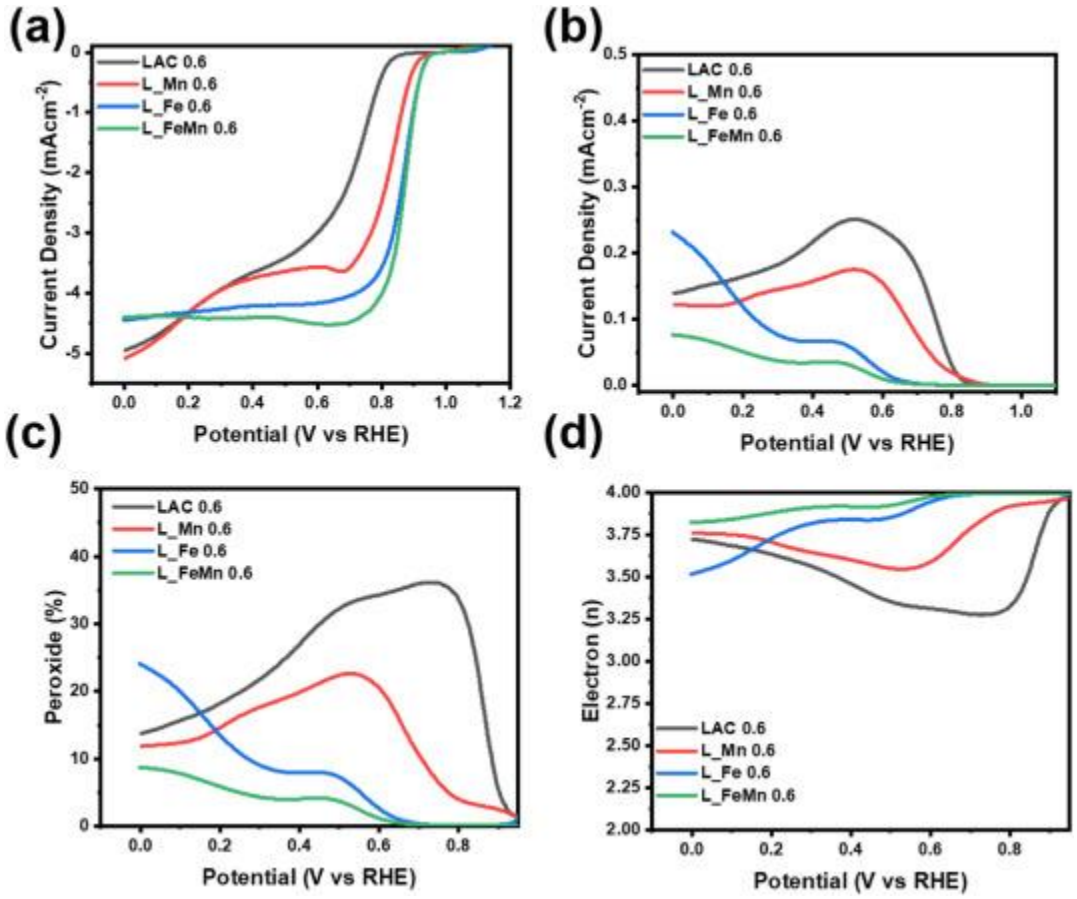

Fig. 5. RRDE measurements of the developed electrocatalysts in O_2-saturated 0.1 M KOH at 1600 rpm with electrocatalyst loading of 0.6 mg cm^{-2}. ORR LSVs obtained at 5 mV s^{-1} (a), ring current densities (b), peroxide yield (c) and the number of electrons (d) transferred during ORR.

3.4.2. ORR performance in acid media

The efficacy of the developed electrocatalysts was additionally probed in acidic conditions comprising of O_2-rich 0.5 M H_2SO_4, again using two different loadings of 0.6 mg cm^{-2} (Fig. 6) and 0.2 mg cm^{-2} (Fig. S6). In acidic conditions, L_Fe with 0.6 mg cm^{-2} loading exhibited E_{onset} and $E_{1/2}$ at 0.84 V (vs RHE) and 0.77 V (vs RHE), respectively, while the I_{limit} came out to be relatively lower. Whereas L_FeMn with an E_{onset} of 0.82 V (vs RHE) showed the maximum I_{limit}. Again L_Mn demonstrated the least activity among the MPc functionalized samples, confirming the inevitability of Fe for carrying out ORR with superior kinetics. Electron transfer number and peroxide yield remained nearly the same for both L_Fe and L_FeMn. Both yielded peroxide ~11–12% while maintaining the nearly tetra-electronic pathway where the electrons transfer came out to be above 3.75. Similar to alkaline situations, a positive influence of electrocatalyst loading on the ORR performance was observed and again higher loading not only improved the kinetics but also effectively decreased the peroxide yield.

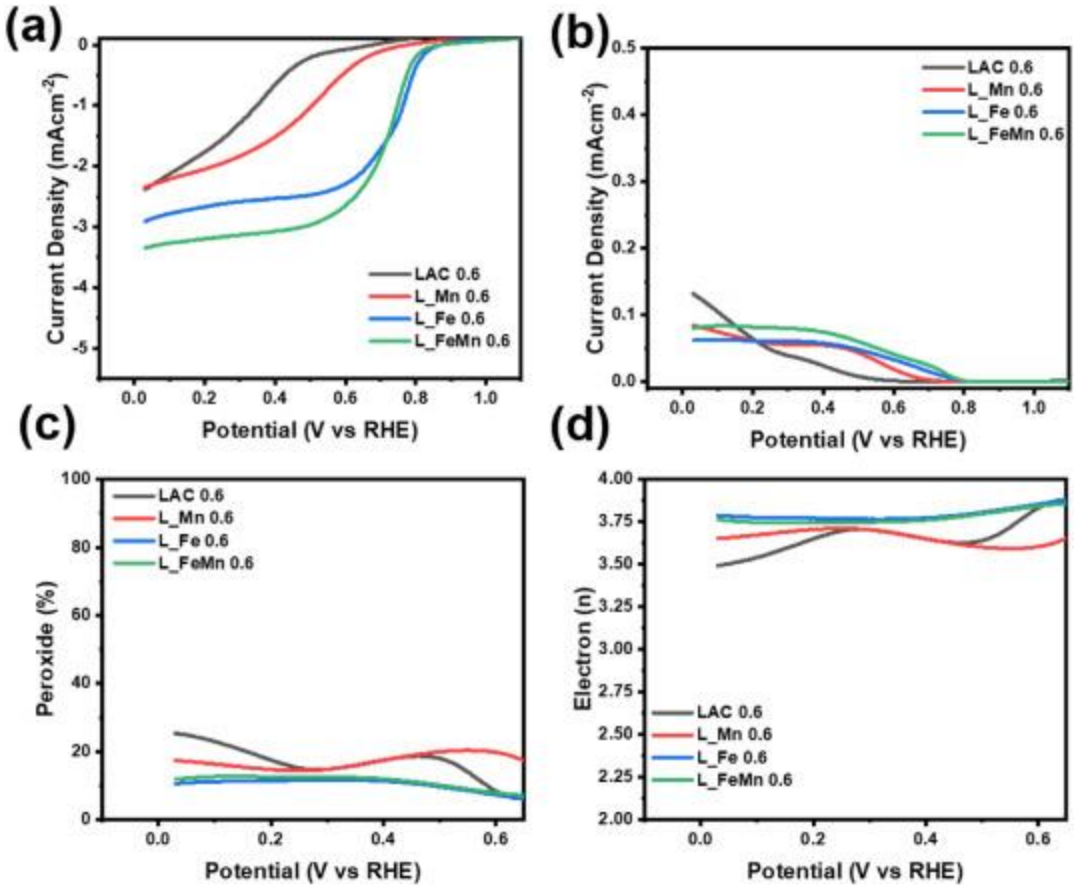

Fig. 6. RRDE measurements of the developed electrocatalysts in O_2-saturated 0.5 M H_2SO_4 at 1600 rpm with electrocatalyst loading of 0.6 mg cm^{-2}. ORR LSVs obtained at 5 mV s^{-1} (a), ring current densities (b), peroxide yield (c) and the number of electrons (d) transferred during ORR.

3.4.3. Electrochemical stability

Overall electrocatalytic activity of the L_Fe and L_FeMn turn out to be comparable where L_FeMn exhibited relatively lower peroxide yield, particularly in alkaline media. While comparing different sorts of monometallic and bimetallic M-N-Cs, Lilloja et al. also experienced the best performance exhibited by Fe-containing monometallic and FeMn bimetallic electrocatalysts [52]. Electrocatalytic activity of L_Fe and L_FeMn could be attributed to structural defects as revealed by Raman, porous carbonaceous architecture visible in TEM micrograph along with the coexistence of different nitrogen moieties confirmed by XPS. Furthermore, microstructural analysis negated the possible agglomeration or nanoparticle formation of metallic species in both samples and endorsed the homogeneous distribution at the atomic level. Moreover, lower production of peroxide with satisfactory kinetics of L_FeMn can be accredited to the synergic effect of Fe and Mn [40,41,[50], [51], [52]].

Along with favorable kinetics and desired selectivity, operational durability is an essential criterion to be fulfilled by the electrocatalysts. For this reason, accelerated stability tests for L_Fe and L_FeMn have been performed over 5000 continuous cycles at 50 mV s^{-1}. From Fig. 7, in an alkaline environment, reasonable stability of $E_{1/2}$ for both electrocatalysts can be acknowledged, however, a negative shift in I_{limit} can be clearly seen. At the potential of 0.4 V, I_{limit} of L_Fe was diminished by 0.59 mA cm^{-2} while I_{limit} of L_FeMn was lowered from 3.97 to 3.17 mA cm^{-2} by the 5000th cycle but still remained categorically higher than that of L_Fe. The obvious impact of this observation can be speculated on the peroxide yield and the number of electrons transferred during ORR. In the case of L_Fe, peroxide production was increased from 10.1% to 20.12% whereas in L_FeMn the undesirable increment in peroxide was restricted to 18.5% at 0.4 V. However, both electrocatalysts demonstrated nearly tetra-electronic reduction of oxygen where electron transfer number persisted above 3.5. Overall, the durability aspects of both electrocatalysts remained more or less the same however, L_FeMn demonstrated a relatively higher I_{limit} and slightly lesser uplift in the yield of peroxide over continuous cycling. The satisfactory robustness of L_FeMn encouraged the execution of stability measurements additionally in the acidic conditions i.e. O_2-saturated 0.5 M H_2SO_4 and achieved trends are illustrated in Fig. S7. In the acidic electrolyte, the electrocatalyst didn't exhibit appreciable durability where both $E_{1/2}$ and I_{limit} were considerably affected as the cycles proceeded. By the end of the stability test, L_FeMn was left with insufficient electrocatalytic activity. The instability of PGM-free electrocatalysts in electrocatalytic media is known and there could be various complex factors damaging the durability including demetalation, deterioration of active moieties, carbon oxidation and so on [107,108]. However, analyzing the exact mechanism behind the limited stability in acidic conditions is somehow beyond the scope of the current study.

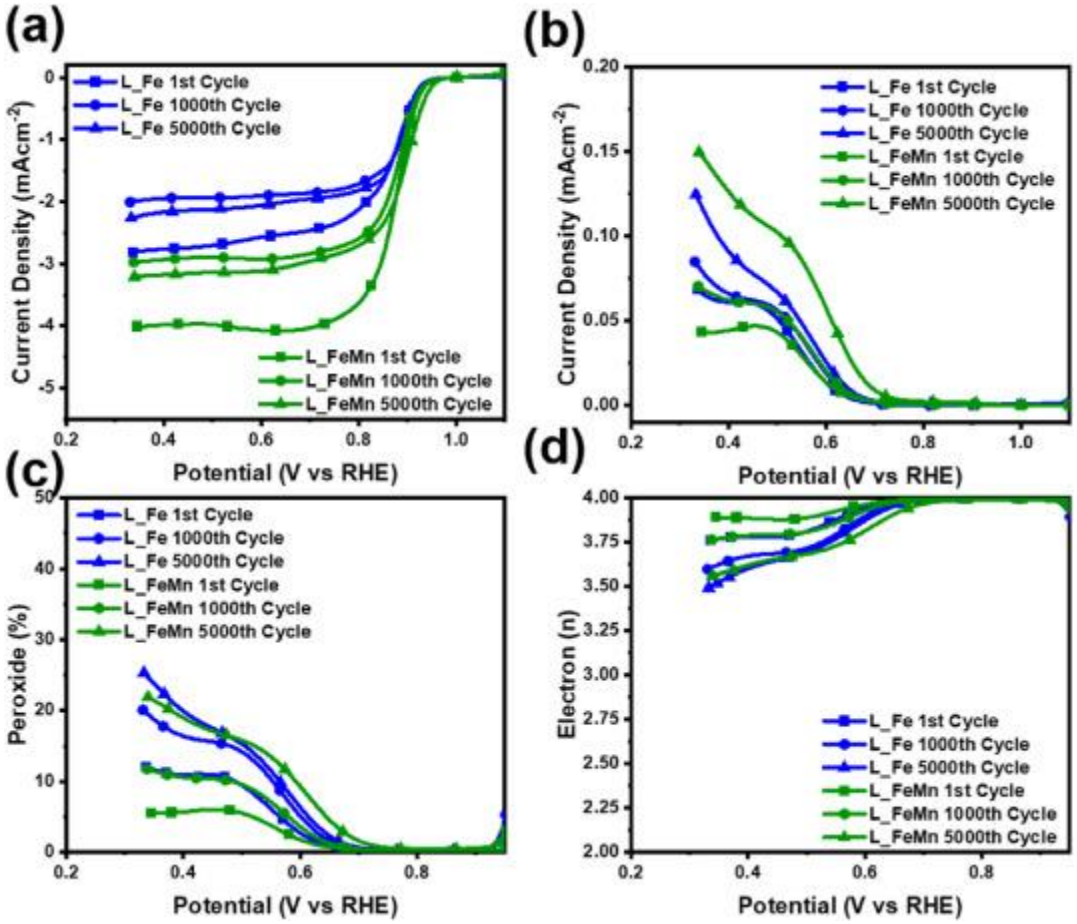

Fig. 7. Illustrates the stability trends over the 5000 cycles in O_2-saturated 0.1 M KOH with 0.6 mg cm^{-2} loading of L_Fe and L_FeMn on RRDE. ORR LSVs obtained at 5 mV s^{-1} (a), ring current densities (b), peroxide yield (c) and the number of electrons (d) transferred during ORR.

3.4.4. Fuel cell testing

Owing to appreciable electro-kinetics and stability demonstrated by L_FeMn during the RRDE measurements, the sample was finally configured as a cathode electrocatalyst to perform ORR in the running FCs. Full device characterizations were implemented to affirm the practicality of L_FeMn for cathode applications in both AEMFC and PEMFC. From Fig. 8a, the performance of AEMFC configured with L_FeMn containing cathode can be acknowledged. AEMFC operating with a feed of pure O_2 (0.6 L min^{-1}) at 60 °C delivered an open circuit voltage (OCV) of 0.893 V. A peak power density (P_{max}) of 261 mW cm^{-2} was observed at the current density of ~577 mA cm^{-2}. On the other hand, when L_FeMn was integrated as an ORR electrocatalyst in the cathodic configuration of PEMFC the performance was not as good as that of AEMFC, indicating that these electrocatalysts can be better employed in the alkaline environment rather than acidic environment. PEMFC was assembled with NR-211 Nafion membrane where the air was fed at the cathode operating at 80 °C.

As can be seen in Fig. 8b, PEMFC exhibited OCV of 0.88 V with P_{max} of ~72 mW cm^{-2} at the current density of ~292 mA cm^{-2}.

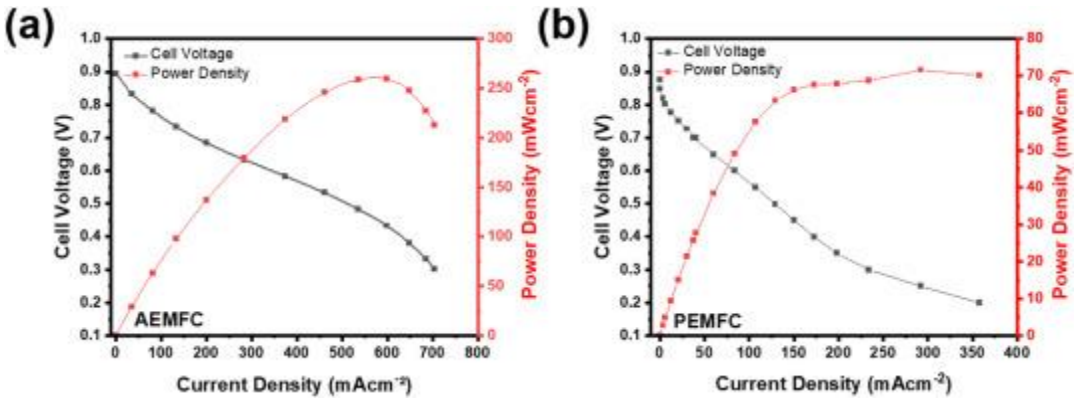

Fig. 8. Full device characterization using L_FeMn as cathode electrocatalyst to perform ORR in (a) AEMFC and (b) PEMFC.

Reasonable outcomes in AEMFC are consistent with the outstanding ORR activity of L_FeMn in the alkaline media during the half-cell testing, confirming the utility of waste biomass-derived electrocatalysts for FC applications. In spite of the fact that a true comparison with previously reported results is a bit difficult task due to variations in the designing parameters of materials and operating conditions [[109], [110], [111]], the obtained AEMFC performance with L_FeMn is comparable to some earlier reports. Very recently, Teppor and coworkers utilized decomposed peat as a carbon precursor for synthesizing PGM-free ORR electrocatalyst and obtained P_{max} of 51 mW cm^{-2} when deployed as a cathode catalyst in AEMFC [112]. Not long ago, Lilloja et al. reported Fe–N–C electrocatalyst prepared using VariPore™ method by Pajarito Powder which demonstrated P_{max} of 220 mW cm^{-2} when applied in AEMFC containing HMT-PMBI membrane [113]. Similarly, Hao et al. prepared multiple metals and heteroatom self-doped biomass-derived electrocatalyst which performed outstandingly during the half-cell analyses in both acidic and alkaline media, however, while used as an air-breathing PEMFC cathode it delivered 17.6 mW cm^{-2} with an OCV of 0.966 V [114]. Moreover, by the virtue of high-temperature pyrolysis, Lilloja et al. produced various monometallic and bimetallic M-N-C for ORR activity in AEMFCs. They observed identical behavior of monometallic Fe–N-MPC and bimetallic FeMn–N-MPC during the RRDE measurements together with outstanding P_{max} of 473 and 474 mW cm^{-2}, respectively, in AEMFC.

Although our full device performances are still inferior to what could be obtained using state-of-the-art electrocatalysts as indicated in the literature [110,[115], [116], [117], [118], [119], [120], [121], [122], [123]], the usage of waste biomass for the

fabrication of cost-effective and efficient electrocatalysts presents a novel pathway under the framework of the circular economy. Despite the promising performance of advanced ORR electrocatalysts, their realistic employment for mass-scale FC applications is limited due to the involvement of the high cost and synthetic complexity of carbon-based materials i.e. carbon nanotubes and graphene-based materials [124]. Whereas the pyrolysis of largely available waste biomass not only provides a sustainable alternative for the cost-effective development of carbon-based electrocatalysts for green energy storage applications but also presents an effective strategy for waste recycling and environmental safety.

4. Conclusion

Lignin, being waste biomass of negligible economical worth, was used to first produce activated char containing networked porosity. Afterward, it was functionalized with FePc and MnPc through a simplistic pyrolysis process in order to fabricate monometallic and bimetallic electrocatalysts. The developed electrocatalysts demonstrated defect-rich porous structures without any substitutional agglomeration in the form of metallic nanoparticles. XPS confirmed the presence of a variety of nitrogen-containing active moieties. RRDE measurements in both alkaline and acidic media with two different loading of $0.2\ mg\ cm^{-2}$ and $0.6\ mg\ cm^{-2}$ validated the active nature of the derived electrocatalysts. In alkaline media, L_Fe and L_FeMn showed outstanding E_{onset} of ∼0.942 V together with an $E_{1/2}$ of 0.874 V. L_FeMn showed decidedly lower peroxide yield with a clear tetra-electronic electro-reduction of O_2 in 0.1 M KOH and also qualified for operational stability. Electrocatalytic performance L_Fe can be linked to the favorable morphological attributes and coexistence of desired nitrogen moieties. While the subsequent reduction in peroxide yield could be additionally attributed synergistic of Fe and Mn. On the other hand, under acidic conditions, L_FeMn had a slightly lower E_{onset} (0.817 V) than that of L_Fe (0.837 V). Contrary to 0.1 M KOH, the durability of L_FeMn was severely affected in 0.5 M H_2SO_4 over the 5000 cycles. Finally, to affirm the realistic utility of L_FeMn for ORR in FCs it was configured as a cathode electrocatalyst in both PEMFC and AEMFC which delivered P_{max} of ∼72 mW cm^{-2} (at 292 mA cm^{-2}) and 261 mW cm^{-2} (at ∼577 mA cm^{-2}), respectively. Last but not the least, this works signposts the new avenues for the cost-effective development of waste-derived M-N-Cs for lethargic ORR in a circular way.

CRediT authorship contribution statement

Mohsin Muhyuddin: Conceptualization, Investigation, Writing – original draft, Methodology, Data curation, Formal analysis, Writing – review & editing. **Ariel Friedman:** Investigation, Writing –

original draft, Methodology, Data curation, Formal analysis. **Federico Poli:** Investigation, Methodology, Data curation, Formal analysis. **Elisabetta Petri:** Investigation, Writing – original draft, Methodology, Data curation, Formal analysis. **Hilah Honig:** Investigation, Writing – original draft, Methodology, Data curation, Formal analysis, Writing – review & editing. **Francesco Basile:** Investigation, Methodology, Resources. **Andrea Fasolini:** Investigation, Methodology, Resources. **Roberto Lorenzi:** Investigation, Writing – original draft, Data curation, Formal analysis. **Enrico Berretti:** Investigation, Writing – original draft, Data curation, Formal analysis. **Marco Bellini:** Investigation, Writing – original draft, Data curation, Formal analysis. **Alessandro Lavacchi:** Funding acquisition, Resources, Supervision, Writing – original draft, Writing – review & editing. **Lior Elbaz:** Funding acquisition, Resources, Supervision, Writing – original draft, Writing – review & editing. **Carlo Santoro:** Conceptualization, Resources, Funding acquisition, Supervision, Writing – original draft, Writing – review & editing. **Francesca Soavi:** Conceptualization, Resources, Funding acquisition, Supervision, Writing – original draft, Writing – review & editing.

Declaration of competing interest

The authors declare that they have no known competing financial interests or personal relationships that could have appeared to influence the work reported in this paper.

Acknowledgments

C.S. would like to thank the support from the Italian Ministry of University and Research (Ministero dell'Università e della Ricerca – MUR) through the "Rita Levi Montalcini 2018" fellowship (Grant number PGR18MAZLI). The authors also thank the Italian ministry MIUR for funding through the FISR 2019 project AMPERE (FISR2019_01294). University of Bologna authors acknowledge MUR and UE support under the project "ECOSYSTEM FOR SUSTAINABLE TRANSITION IN EMILIA-ROMAGNA" of the National Recovery and Resilience Plan (NRRP-PNRR).

References

[1] H. Zhang, H. Osgood, X. Xie, Y. Shao, G. Wu, Engineering nanostructures of PGM-free oxygen-reduction catalysts using metal-organic frameworks, Nano Energy 31 (2017) 331–350, https://doi.org/10.1016/j.nanoen.2016.11.033.

[2] M.K. Debe, Electrocatalyst approaches and challenges for automotive fuel cells, Nature 486 (2012) 43–51, https://doi.org/10.1038/nature11115.

[3] Y. He, S. Liu, C. Priest, Q. Shi, G. Wu, Atomically dispersed metal–nitrogen–carbon catalysts for fuel cells: advances in catalyst design, electrode performance, and durability improvement, Chem. Soc. Rev. 49 (2020) 3484–3524, https://doi.org/10.1039/C9CS00903E.
[4] N. Ramaswamy, S. Mukerjee, Fundamental mechanistic understanding of electrocatalysis of oxygen reduction on Pt and non-Pt surfaces: acid versus alkaline media, Adv. Phys. Chem. (2012) 2012, https://doi.org/10.1155/2012/491604.
[5] Y. Nie, L. Li, Z. Wei, Recent advancements in Pt and Pt-free catalysts for oxygen reduction reaction, Chem. Soc. Rev. 44 (2015) 2168–2201, https://doi.org/10.1039/C4CS00484A.
[6] R. Ma, G. Lin, Y. Zhou, Q. Liu, T. Zhang, G. Shan, M. Yang, J. Wang, A review of oxygen reduction mechanisms for metal-free carbon-based electrocatalysts, Npj Comput Mater 5 (2019) 1–15, https://doi.org/10.1038/s41524-019-0210-3.
[7] A. Muthukrishnan, Y. Nabae, T. Ohsaka, Role of iron in the reduction of H2O2 intermediate during the oxygen reduction reaction on iron-containing polyimide-based electrocatalysts, RSC Adv. 6 (2016) 3774–3777, https://doi.org/10.1039/C5RA23162K.
[8] X. Zhao, Y. Liu, Origin of selective production of hydrogen peroxide by electrochemical oxygen reduction, J. Am. Chem. Soc. 143 (2021) 9423–9428, https://doi.org/10.1021/jacs.1c02186.
[9] J. Huang, Q. Lu, X. Ma, X. Yang, Bio-inspired FeN5 moieties anchored on a three-dimensional graphene aerogel to improve oxygen reduction catalytic performance, J. Mater. Chem. A. 6 (2018) 18488–18497, https://doi.org/10.1039/C8TA06455E.
[10] S. Guo, S. Zhang, S. Sun, Tuning nanoparticle catalysis for the oxygen reduction reaction, Angew. Chem. Int. Ed. 52 (2013) 8526–8544, https://doi.org/10.1002/anie.201207186.
[11] U. Tylus, Q. Jia, H. Hafiz, R.J. Allen, B. Barbiellini, A. Bansil, S. Mukerjee, Engendering anion immunity in oxygen consuming cathodes based on Fe-Nx electrocatalysts: spectroscopic and electrochemical advanced characterizations, Appl. Catal. B: Environ. 198 (2016) 318–324, https://doi.org/10.1016/j.apcatb.2016.05.054.
[12] Y. He, Q. Tan, L. Lu, J. Sokolowski, G. Wu, Metal-nitrogen-carbon catalysts for

oxygen reduction in PEM fuel cells: self-template synthesis approach to enhancing catalytic activity and stability, Electrochem. Energy Rev. 2 (2019), https://doi.org/10.1007/s41918-019-00031-9.
[13] S. Specchia, P. Atanassov, J.H. Zagal, Mapping transition metal–nitrogen–carbon catalyst performance on the critical descriptor diagram, Curr. Opin. Electrochem. 27 (2021), 100687, https://doi.org/10.1016/j.coelec.2021.100687.
[14] M. Shen, C. Wei, K. Ai, L. Lu, Transition metal–nitrogen–carbon nanostructured catalysts for the oxygen reduction reaction: from mechanistic insights to structural optimization, Nano Res. 10 (2017) 1449–1470, https://doi.org/10.1007/s12274-016-1400-7.
[15] M.-X. Chen, L. Tong, H.-W. Liang, Understanding the catalytic sites of metal–nitrogen–carbon oxygen reduction electrocatalysts, Chem. Eur J. 27 (2021) 145–157, https://doi.org/10.1002/chem.202002427.
[16] K. Singh, F. (Sanaz, J.-S. Yu Razmjooei, Active sites and factors influencing them for efficient oxygen reduction reaction in metal-N coordinated pyrolyzed and non-pyrolyzed catalysts: a review, J. Mater. Chem. A. 5 (2017), https://doi.org/10.1039/C7TA05222G.
[17] C. Liu, H. Li, F. Liu, J. Chen, Z. Yu, Z. Yuan, C. Wang, H. Zheng, G. Henkelman, L. Wei, Y. Chen, Intrinsic activity of metal centers in metal–nitrogen–carbon single-atom catalysts for hydrogen peroxide synthesis, J. Am. Chem. Soc. 142 (2020) 21861–21871, https://doi.org/10.1021/jacs.0c10636.
[18] P. Trogadas, T. Fuller, P. Strasser, Carbon as catalyst and support for electrochemical energy conversion, Carbon 75 (2014) 5–42, https://doi.org/10.1016/j.carbon.2014.04.005.
[19] D. Yan, Y. Li, J. Huo, R. Chen, L. Dai, S. Wang, Defect chemistry of nonprecious-metal electrocatalysts for oxygen reactions, Adv. Mater. 29 (2017), 1606459, https://doi.org/10.1002/adma.201606459.
[20] J. He, T. Zheng, D. Wu, S. Zhang, M. Gu, Q. He, Insights into the determining effect of carbon support properties on anchoring active sites in Fe–N–C catalysts toward the oxygen reduction reaction, ACS Catal. 12 (2022) 1601–1613, https://doi.org/10.1021/acscatal.1c04815.
[21] L. Yang, J. Shui, L. Du, Y. Shao, J. Liu, L. Dai, Z. Hu, Carbon-based metal-free ORR electrocatalysts for fuel cells: past, present, and future, Adv. Mater. 31 (2019), 1804799, https://doi.org/10.1002/adma.201804799.

[22] O.L. Li, K. Prabakar, A. Kaneko, H. Park, T. Ishizaki, Exploration of Lewis basicity and oxygen reduction reaction activity in plasma-tailored nitrogen-doped carbon electrocatalysts, Catal. Today 337 (2019), https://doi.org/10.1016/j.cattod.2019.02.058.
[23] E. Berretti, M. Longhi, P. Atanassov, D. Sebasti´an, C. Lo Vecchio, V. Baglio, A. Serov, A. Marchionni, F. Vizza, C. Santoro, A. Lavacchi, Platinum group metal-free Fe-based (FeNC) oxygen reduction electrocatalysts for direct alcohol fuel cells, Curr. Opin. Electrochem. 29 (2021), 100756, https://doi.org/10.1016/j.coelec.2021.100756.
[24] C.Z. Loyola, S. Ureta-Za˜nartu, J.H. Zagal, F. Tasca, Activity volcano plots for the oxygen reduction reaction using FeN4 complexes: from reported experimental data to the electrochemical meaning, Curr. Opin. Electrochem. 32 (2022), 100923, https://doi.org/10.1016/j.coelec.2021.100923.
[25] K. Ozoemena, Nanostructured platinum-free electrocatalysts in alkaline direct alcohol fuel cells: catalyst design, principles and applications, RSC Adv. 6 (2016), https://doi.org/10.1039/C6RA15057H.
[26] J.H. Zagal, I. Ponce, R. O˜nate, Redox Potentials as Reactivity Descriptors in Electrochemistry, IntechOpen, 2019, https://doi.org/10.5772/intechopen.89883.
[27] U. Tylus, Q. Jia, K. Strickland, N. Ramaswamy, A. Serov, P. Atanassov, S. Mukerjee, Elucidating oxygen reduction active sites in pyrolyzed metal–nitrogen coordinated non-precious-metal electrocatalyst systems, J. Phys. Chem. C 118 (2014) 8999–9008, https://doi.org/10.1021/jp500781v.
[28] R. Venegas, F.J. Recio, J. Riquelme, K. Neira, J.F. Marco, I. Ponce, J.H. Zagal, F. Tasca, Biomimetic reduction of O2 in an acid medium on iron phthalocyanines axially coordinated to pyridine anchored on carbon nanotubes, J. Mater. Chem. A. 5 (2017) 12054–12059, https://doi.org/10.1039/C7TA02381B.
[29] A. Kozhushner, N. Zion, L. Elbaz, Methods for assessment and measurement of the active site density in platinum group metal–free oxygen reduction reaction catalysts, Curr. Opin. Electrochem. 25 (2021), 100620, https://doi.org/10.1016/j.coelec.2020.08.002.
[30] Q. Jia, N. Ramaswamy, U. Tylus, K. Strickland, J. Li, A. Serov, K. Artyushkova, P. Atanassov, J. Anibal, C. Gumeci, S.C. Barton, M.-T. Sougrati, F. Jaouen, B. Halevi, S. Mukerjee, Spectroscopic insights into the nature of active sites in

iron–nitrogen–carbon electrocatalysts for oxygen reduction in acid, Nano Energy 29 (2016) 65–82, https://doi.org/10.1016/j.nanoen.2016.03.025.
[31] J.H. Zagal, S. Griveau, J.F. Silva, T. Nyokong, F. Bedioui, Metallophthalocyanine-based molecular materials as catalysts for electrochemical reactions, Coord. Chem. Rev. 254 (2010) 2755–2791, https://doi.org/10.1016/j.ccr.2010.05.001.
[32] J. Zagal, M. P´aez, A.A. Tanaka, J.R. dos Santos, C.A. Linkous, Electrocatalytic activity of metal phthalocyanines for oxygen reduction, J. Electroanal. Chem. 339 (1992) 13–30, https://doi.org/10.1016/0022-0728(92)80442-7.
[33] T. Marshall-Roth, N.J. Libretto, A.T. Wrobel, K.J. Anderton, M.L. Pegis, N. D. Ricke, T.V. Voorhis, J.T. Miller, Y. Surendranath, A pyridinic Fe-N4 macrocycle models the active sites in Fe/N-doped carbon electrocatalysts, Nat. Commun. 11 (2020) 5283, https://doi.org/10.1038/s41467-020-18969-6.
[34] X.X. Wang, M.T. Swihart, G. Wu, Achievements, challenges and perspectives on cathode catalysts in proton exchange membrane fuel cells for transportation, Nat Catal 2 (2019) 578–589, https://doi.org/10.1038/s41929-019-0304-9.
[35] T. Asset, P. Atanassov, Iron-nitrogen-carbon catalysts for proton exchange membrane fuel cells, Joule 4 (2020) 33–44, https://doi.org/10.1016/j.joule.2019.12.002.
[36] U. Martinez, S. Komini Babu, E.F. Holby, H.T. Chung, X. Yin, P. Zelenay, Progress in the development of Fe-based PGM-free electrocatalysts for the oxygen reduction reaction, Adv. Mater. 31 (2019), 1806545, https://doi.org/10.1002/adma.201806545.
[37] Q. Liu, Y. Wang, Z. Hu, Z. Zhang, Iron-based single-atom electrocatalysts: synthetic strategies and applications, RSC Adv. 11 (2021) 3079–3095, https://doi.org/10.1039/D0RA08223F.
[38] J. Li, M.T. Sougrati, A. Zitolo, J.M. Ablett, I.C. O˘guz, T. Mineva, I. Matanovic, P. Atanassov, Y. Huang, I. Zenyuk, A. Di Cicco, K. Kumar, L. Dubau, F. Maillard, G. Dra˘zi´c, F. Jaouen, Identification of durable and non-durable FeNx sites in Fe–N–C materials for proton exchange membrane fuel cells, Nat Catal 4 (2021) 10–19, https://doi.org/10.1038/s41929-020-00545-2.
[39] W. Wang, Q. Jia, S. Mukerjee, S. Chen, Recent insights into the oxygen-reduction electrocatalysis of Fe/N/C materials, ACS Catal. 9 (2019) 10126–10141, https://doi.org/10.1021/acscatal.9b02583.
[40] Y. Kumar, E. Kibena-P˜oldsepp, J. Kozlova, M. R¨ahn, A. Treshchalov, A. Kikas,

V. Kisand, J. Aruv¨ali, A. Tamm, J.C. Douglin, S.J. Folkman, I. Gelmetti, F. A. Garc´es-Pineda, J.R. Gal´an-Mascar´os, D.R. Dekel, K. Tammeveski, Bifunctional oxygen electrocatalysis on mixed metal phthalocyanine-modified carbon nanotubes prepared via pyrolysis, ACS Appl. Mater. Interfaces 13 (2021) 41507–41516, https://doi.org/10.1021/acsami.1c06737.
[41] A. Serov, M.H. Robson, M. Smolnik, P. Atanassov, Templated bi-metallic non-PGM catalysts for oxygen reduction, Electrochim. Acta 80 (2012) 213–218, https://doi.org/10.1016/j.electacta.2012.07.008.
[42] B. Zhong, L. Zhang, J. Yu, K. Fan, Ultrafine iron-cobalt nanoparticles embedded in nitrogen-doped porous carbon matrix for oxygen reduction reaction and zinc-air batteries, J. Colloid Interface Sci. 546 (2019) 113–121, https://doi.org/10.1016/j.jcis.2019.03.038.
[43] W. Ran, J. Dong, T. Sun, J. Chen, L. Xu, Iron, cobalt, and nitrogen tri-doped ordered mesoporous carbon as a highly efficient electrocatalyst for oxygen reduction reaction, ChemistrySelect 4 (2019) 7728–7733, https://doi.org/10.1002/slct.201901641.
[44] W.-K. Jo, S. Moru, D.-E. Lee, S. Tonda, Cobalt- and iron-coordinated graphitic carbon nitride on reduced graphene oxide: a nonprecious bimetallic M–Nx–C analogue electrocatalyst for efficient oxygen reduction reaction in acidic media, Appl. Surf. Sci. 531 (2020), 147367, https://doi.org/10.1016/j.apsusc.2020.147367.
[45] Z. Hu, Z. Guo, Z. Zhang, M. Dou, F. Wang, Bimetal zeolitic imidazolite framework-derived iron-, cobalt- and nitrogen-codoped carbon nanopolyhedra electrocatalyst for efficient oxygen reduction, ACS Appl. Mater. Interfaces 10 (2018) 12651–12658, https://doi.org/10.1021/acsami.8b00512.
[46] R. Mercado, C. Wahl, J. En Lu, T. Zhang, B. Lu, P. Zhang, J.Q. Lu, A. Allen, J. Z. Zhang, S. Chen, Nitrogen-doped porous carbon cages for electrocatalytic reduction of oxygen: enhanced performance with iron and cobalt dual metal centers, ChemCatChem 12 (2020) 3230–3239, https://doi.org/10.1002/cctc.201902324.
[47] Priorities for Critical Materials for a Circular Economy, EASAC – the European Academies' Science Advisory Council, Halle (Saale) Germany, 2016.
[48] I. Directorate-General for Internal Market, S. Bobba, P. Claudiu, D. Huygens, P. Alves Dias, B. Gawlik, E. Tzimas, D. Wittmer, P. Nuss, M. Grohol, H. Saveyn,

F. Buraoui, G. Orveillon, T. H´amor, S. Slavko, F. Mathieux, M. Gislev, C. Torres De Matos, G.A. Blengini, F. Ardente, D. Blagoeva, E. Garbarino, in: Report on Critical Raw Materials and the Circular Economy, Publications Office of the European Union, LU, 2018. https://data.europa.eu/doi/10.2873/167813. (Accessed 7 May 2022).
[49] Y. Sun, L. Silvioli, N.R. Sahraie, W. Ju, J. Li, A. Zitolo, S. Li, A. Bagger, L. Arnarson, X. Wang, T. Moeller, D. Bernsmeier, J. Rossmeisl, F. Jaouen, P. Strasser, Activity–selectivity trends in the electrochemical production of hydrogen peroxide over single-site metal–nitrogen–carbon catalysts, J. Am. Chem. Soc. 141 (2019) 12372–12381, https://doi.org/10.1021/jacs.9b05576.
[50] M. Kodali, C. Santoro, S. Herrera, A. Serov, P. Atanassov, Bimetallic platinum group metal-free catalysts for high power generating microbial fuel cells, J. Power Sources 366 (2017) 18–26, https://doi.org/10.1016/j.jpowsour.2017.08.110.
[51] F. Li, P. Shi, J. Wu, X. Qi, Y. Liu, G. Li, Trace bimetallic iron/manganese Co-doped N-ketjenblack carbon electrocatalyst for robust oxygen reduction reaction, J. Electrochem. Soc. 168 (2021), 060502, https://doi.org/10.1149/1945-7111/ac03f3.
[52] J. Lilloja, E. Kibena-P˜oldsepp, A. Sarapuu, M. K¨a¨arik, J. Kozlova, P. Paiste, A. Kikas, A. Treshchalov, J. Leis, A. Tamm, V. Kisand, S. Holdcroft, K. Tammeveski, Transition metal and nitrogen-doped mesoporous carbons as cathode catalysts for anion-exchange membrane fuel cells, Appl. Catal. B: Environ. 306 (2022), 121113, https://doi.org/10.1016/j.apcatb.2022.121113.
[53] M. Borghei, J. Lehtonen, L. Liu, O.J. Rojas, Advanced biomass-derived electrocatalysts for the oxygen reduction reaction, Adv. Mater. 30 (2018), 1703691, https://doi.org/10.1002/adma.201703691.
[54] M. Wang, S. Wang, H. Yang, W. Ku, S. Yang, Z. Liu, G. Lu, Carbon-based electrocatalysts derived from biomass for oxygen reduction reaction: a minireview, Front. Chem. 8 (2020). https://www.frontiersin.org/article/10.3389/fchem.2020.00116. (Accessed 7 May 2022).
[55] L. Du, G. Zhang, X. Liu, A. Hassanpour, M. Dubois, A.C. Tavares, S. Sun, Biomass-derived nonprecious metal catalysts for oxygen reduction reaction: the demand-oriented engineering of active sites and structures, Carbon Energy 2 (2020) 561–581, https://doi.org/10.1002/cey2.73.
[56] M. Jiang, X. Yu, H. Yang, S. Chen, Optimization strategies of preparation of

biomass-derived carbon electrocatalyst for boosting oxygen reduction reaction: a minireview, Catalysts 10 (2020) 1472, https://doi.org/10.3390/catal10121472.
[57] S. Zago, M. Bartoli, M. Muhyuddin, G.M. Vanacore, P. Jagdale, A. Tagliaferro, C. Santoro, S. Specchia, Engineered biochar derived from pyrolyzed waste tea as a carbon support for Fe-N-C electrocatalysts for the oxygen reduction reaction, Electrochim. Acta 412 (2022), 140128, https://doi.org/10.1016/j.electacta.2022.140128.
[58] J. Munuera, L. Britnell, C. Santoro, R. Cu´ellar-Franca, C. Casiraghi, A review on sustainable production of graphene and related life cycle assessment, 2D Mater. 9 (2021), 012002, https://doi.org/10.1088/2053-1583/ac3f23.
[59] B.K. Mutuma, N.F. Sylla, A. Bubu, N.M. Ndiaye, C. Santoro, A. Brilloni, F. Poli, N. Manyala, F. Soavi, Valorization of biodigestor plant waste in electrodes for supercapacitors and microbial fuel cells, Electrochim. Acta 391 (2021), 138960, https://doi.org/10.1016/j.electacta.2021.138960.
[60] M. Muhyuddin, P. Mustarelli, C. Santoro, Recent advances in waste plastic transformation into valuable platinum-group metal-free electrocatalysts for oxygen reduction reaction, ChemSusChem 14 (2021) 3785–3800, https://doi.org/10.1002/cssc.202101252.
[61] N. Cai, H. Yang, X. Zhang, S. Xia, D. Yao, P. Bartocci, F. Fantozzi, Y. Chen, H. Chen, P.T. Williams, Bimetallic carbon nanotube encapsulated Fe-Ni catalysts from fast pyrolysis of waste plastics and their oxygen reduction properties, Waste Manag. 109 (2020) 119–126, https://doi.org/10.1016/j.wasman.2020.05.003.
[62] N. Cai, S. Xia, X. Zhang, Z. Meng, P. Bartocci, F. Fantozzi, Y. Chen, H. Chen, P. T. Williams, H. Yang, Preparation of iron- and nitrogen-codoped carbon nanotubes from waste plastics pyrolysis for the oxygen reduction reaction, ChemSusChem 13 (2020) 938–944, https://doi.org/10.1002/cssc.201903293.
[63] G. Daniel, T. Kosmala, M.C. Dalconi, L. Nodari, D. Badocco, P. Pastore, A. Lorenzetti, G. Granozzi, C. Durante, Upcycling of polyurethane into iron-nitrogen-carbon electrocatalysts active for oxygen reduction reaction, Electrochim. Acta 362 (2020), 137200, https://doi.org/10.1016/j.electacta.2020.137200.
[64] M. Muhyuddin, J. Filippi, L. Zoia, S. Bonizzoni, R. Lorenzi, E. Berretti, L. Capozzoli, M. Bellini, C. Ferrara, A. Lavacchi, C. Santoro, Waste face surgical mask transformation into crude oil and nanostructured electrocatalysts for fuel

cells and electrolyzers, ChemSusChem 15 (2022), e202102351, https://doi.org/10.1002/cssc.202102351.
[65] Converting Waste Agricultural Biomass into a Resource-Compendium of Technologies, United Nations Environmental Programme, Japan, 2009. https://wedocs.unep.org/xmlui/handle/20.500.11822/7614. (Accessed 7 May 2022).
[66] H. Zhou, T. Fan, D. Zhang, Biotemplated materials for sustainable energy and environment: current status and challenges, ChemSusChem 4 (2011) 1344–1387, https://doi.org/10.1002/cssc.201100048.
[67] D.L. Klass, Biomass for Renewable Energy, Fuels, and Chemicals, Elsevier, 1998.
[68] M. Garedew, F. Lin, B. Song, T.M. DeWinter, J.E. Jackson, C.M. Saffron, C.H. Lam, P.T. Anastas, Greener routes to biomass waste valorization: lignin transformation through electrocatalysis for renewable chemicals and fuels production, ChemSusChem 13 (2020) 4214–4237, https://doi.org/10.1002/cssc.202000987.
[69] H.Y. Lim, S. Yusup, A.C.M. Loy, S. Samsuri, S.S.K. Ho, A.S.A. Manaf, S.S. Lam, B.L. F. Chin, M.N. Acda, P. Unrean, E. Rianawati, Review on conversion of lignin waste into value-added Resources in tropical countries, Waste Biomass Valor 12 (2021) 5285–5302, https://doi.org/10.1007/s12649-020-01307-8.
[70] D.S. Bajwa, G. Pourhashem, A.H. Ullah, S.G. Bajwa, A concise review of current lignin production, applications, products and their environmental impact, Ind. Crop. Prod. 139 (2019), 111526, https://doi.org/10.1016/j.indcrop.2019.111526.
[71] I. Haq, P. Mazumder, A.S. Kalamdhad, Recent advances in removal of lignin from paper industry wastewater and its industrial applications – a review, Bioresour. Technol. 312 (2020), 123636, https://doi.org/10.1016/j.biortech.2020.123636.
[72] M. Bellini, M.V. Pagliaro, A. Lenarda, P. Fornasiero, M. Marelli, C. Evangelisti, M. Innocenti, Q. Jia, S. Mukerjee, J. Jankovic, L. Wang, J.R. Varcoe, C. B. Krishnamurthy, I. Grinberg, E. Davydova, D.R. Dekel, H.A. Miller, F. Vizza, Palladium–ceria catalysts with enhanced alkaline hydrogen oxidation activity for anion exchange membrane fuel cells, ACS Appl. Energy Mater. 2 (2019) 4999–5008, https://doi.org/10.1021/acsaem.9b00657.
[73] H.A. Miller, M.V. Pagliaro, M. Bellini, F. Bartoli, L. Wang, I. Salam, J.R. Varcoe, F. Vizza, Integration of a Pd-CeO2/C anode with Pt and Pt-free cathode catalysts in high power density anion exchange membrane fuel cells, ACS Appl. Energy Mater. 3 (2020) 10209–10214, https://doi.org/10.1021/acsaem.0c01998.

[74] L. Wang, X. Peng, W.E. Mustain, J.R. Varcoe, Radiation-grafted anion-exchange membranes: the switch from low- to high-density polyethylene leads to remarkably enhanced fuel cell performance, Energy Environ. Sci. 12 (2019) 1575–1579, https://doi.org/10.1039/C9EE00331B.
[75] S. Liu, L. Liu, X. Chen, Z. Yang, M. Li, Y. Wang, W. Lv, P. Zhu, X. Zhao, G. Wang, On an easy way to prepare Fe, S, N tri-doped mesoporous carbon materials as efficient electrocatalysts for oxygen reduction reaction, Electrocatalysis 10 (2019) 72–81, https://doi.org/10.1007/s12678-018-0496-9.
[76] C. Zhu, Q. Shi, B. Xu, S. Fu, G. Wan, C. Yang, S. Yao, J. Song, H. Zhou, D. Du, S. Beckman, D. Su, Y. Lin, Hierarchically porous M-N-C (M = Co and Fe) single-atom electrocatalysts with robust MN x active moieties enable enhanced ORR performance, Adv. Energy Mater. 8 (2018), 1801956, https://doi.org/10.1002/aenm.201801956.
[77] T. Liu, F. Sun, M. Huang, L. Guan, Atomically dispersed Co–N–C electrocatalysts synthesized by a low-speed ball milling method for proton exchange membrane fuel cells, Mater. Adv. 3 (2022) 1565–1573, https://doi.org/10.1039/D1MA00809A.
[78] X. Luo, X. Wei, H. Wang, W. Gu, T. Kaneko, Y. Yoshida, X. Zhao, C. Zhu, Secondary-atom-doping enables robust Fe–N–C single-atom catalysts with enhanced oxygen reduction reaction, Nano-Micro Lett. 12 (2020) 163, https://doi.org/10.1007/s40820-020-00502-5.
[79] C. Xin, W. Shang, J. Hu, C. Zhu, J. Guo, J. Zhang, H. Dong, W. Liu, Y. Shi, Integration of morphology and electronic structure modulation on atomic iron-nitrogen-carbon catalysts for highly efficient oxygen reduction, Adv. Funct. Mater. 32 (2022), https://doi.org/10.1002/adfm.202108345.
[80] H. Yang, L. Shang, Q. Zhang, R. Shi, G. Waterhouse, L. Gu, T. Zhang, A universal ligand mediated method for large scale synthesis of transition metal single atom catalysts, Nat. Commun. 10 (2019) 1–9, https://doi.org/10.1038/s41467-019-12510-0.
[81] A.C. Ferrari, J. Robertson, Interpretation of Raman spectra of disordered and amorphous carbon, Phys. Rev. B 61 (2000) 14095–14107, https://doi.org/10.1103/PhysRevB.61.14095.
[82] L.G. Cançado, A. Jorio, E.H.M. Ferreira, F. Stavale, C.A. Achete, R.B. Capaz, M.V. O. Moutinho, A. Lombardo, T.S. Kulmala, A.C. Ferrari, Quantifying defects in

graphene via Raman spectroscopy at different excitation energies, Nano Lett. 11 (2011) 3190–3196, https://doi.org/10.1021/nl201432g.
[83] C. Casimero, C. Hegarty, R.J. McGlynn, J. Davis, Ultrasonic exfoliation of carbon fiber: electroanalytical perspectives, J. Appl. Electrochem. 50 (2020) 383–394, https://doi.org/10.1007/s10800-019-01379-y.
[84] B.J. Matsoso, K. Ranganathan, B.K. Mutuma, T. Lerotholi, G. Jones, N.J. Coville, Time-dependent evolution of the nitrogen configurations in N-doped graphene films, RSC Adv. 6 (2016) 106914–106920, https://doi.org/10.1039/C6RA24094A.
[85] L.M. Malard, M.A. Pimenta, G. Dresselhaus, M.S. Dresselhaus, Raman spectroscopy in graphene, Phys. Rep. 473 (2009) 51–87, https://doi.org/10.1016/j.physrep.2009.02.003.
[86] P. Song, M. Luo, X. Liu, W. Xing, W. Xu, Z. Jiang, L. Gu, Zn single atom catalyst for highly efficient oxygen reduction reaction, Adv. Funct. Mater. 27 (2017), 1700802, https://doi.org/10.1002/adfm.201700802.
[87] J. Wang, F. Ciucci, Boosting bifunctional oxygen electrolysis for N-doped carbon via bimetal addition, Small 13 (2017), 1604103, https://doi.org/10.1002/smll.201604103.
[88] K. Artyushkova, A. Serov, S. Rojas-Carbonell, P. Atanassov, Chemistry of multitudinous active sites for oxygen reduction reaction in transition metal–nitrogen–carbon electrocatalysts, J. Phys. Chem. C 119 (2015) 25917–25928, https://doi.org/10.1021/acs.jpcc.5b07653.
[89] C. Santoro, P. Bollella, B. Erable, P. Atanassov, D. Pant, Oxygen reduction reaction electrocatalysis in neutral media for bioelectrochemical systems, Nat Catal 5 (2022) 473–484, https://doi.org/10.1038/s41929-022-00787-2.
[90] P. Lazar, R. Mach, M. Otyepka, Spectroscopic fingerprints of graphitic, pyrrolic, pyridinic, and chemisorbed nitrogen in N-doped graphene, J. Phys. Chem. C 123 (2019) 10695–10702, https://doi.org/10.1021/acs.jpcc.9b02163.
[91] K. Artyushkova, Misconceptions in interpretation of nitrogen chemistry from x-ray photoelectron spectra, J. Vac. Sci. Technol. 38 (2020), 031002, https://doi.org/10.1116/1.5135923.
[92] M. Kodali, C. Santoro, A. Serov, S. Kabir, K. Artyushkova, I. Matanovic, P. Atanassov, Air breathing cathodes for microbial fuel cell using Mn-, Fe-, Co- and Ni-containing platinum group metal-free catalysts, Electrochim. Acta 231

(2017) 115–124, https://doi.org/10.1016/j.electacta.2017.02.033.
[93] M.J. Dzara, K. Artyushkova, S. Shulda, M.B. Strand, C. Ngo, E.J. Crumlin, T. Gennett, S. Pylypenko, Characterization of complex interactions at the gas–solid interface with in situ spectroscopy: the case of nitrogen-functionalized carbon, J. Phys. Chem. C 123 (2019) 9074–9086, https://doi.org/10.1021/acs.jpcc.9b00487.
[94] S. Kabir, K. Artyushkova, A. Serov, P. Atanassov, Role of nitrogen moieties in N-doped 3D-graphene nanosheets for oxygen electroreduction in acidic and alkaline media, ACS Appl. Mater. Interfaces 10 (2018) 11623–11632, https://doi.org/10.1021/acsami.7b18651.
[95] C. Santoro, S. Rojas-Carbonell, R. Awais, R. Gokhale, M. Kodali, A. Serov, K. Artyushkova, P. Atanassov, Influence of platinum group metal-free catalyst synthesis on microbial fuel cell performance, J. Power Sources 375 (2018) 11–20, https://doi.org/10.1016/j.jpowsour.2017.11.039.
[96] T. Okada, K.Y. Inoue, G. Kalita, M. Tanemura, T. Matsue, M. Meyyappan, S. Samukawa, Bonding state and defects of nitrogen-doped graphene in oxygen reduction reaction, Chem. Phys. Lett. 665 (2016) 117–120, https://doi.org/10.1016/j.cplett.2016.10.061.
[97] L. Lai, J.R. Potts, D. Zhan, L. Wang, C.K. Poh, C. Tang, H. Gong, Z. Shen, J. Lin, R. S. Ruoff, Exploration of the active center structure of nitrogen-doped graphene-based catalysts for oxygen reduction reaction, Energy Environ. Sci. 5 (2012) 7936–7942, https://doi.org/10.1039/C2EE21802J.
[98] I. Matanovic, K. Artyushkova, P. Atanassov, Understanding PGM-free catalysts by linking density functional theory calculations and structural analysis: perspectives and challenges, Curr. Opin. Electrochem. 9 (2018) 137–144, https://doi.org/10.1016/j.coelec.2018.03.009.
[99] S. Rojas-Carbonell, K. Artyushkova, A. Serov, C. Santoro, I. Matanovic, P. Atanassov, Effect of pH on the activity of platinum group metal-free catalysts in oxygen reduction reaction, ACS Catal. 8 (2018) 3041–3053, https://doi.org/10.1021/acscatal.7b03991.
[100] A. Serov, K. Artyushkova, P. Atanassov, Fe-N-C oxygen reduction fuel cell catalyst derived from carbendazim: synthesis, structure, and reactivity, Adv. Energy Mater. 4 (2014), 1301735, https://doi.org/10.1002/aenm.201301735.
[101] R. Sgarbi, K. Kumar, F. Jaouen, A. Zitolo, E.A. Ticianelli, F. Maillard, Oxygen

reduction reaction mechanism and kinetics on M-NxCy and M@N-C active sites present in model M-N-C catalysts under alkaline and acidic conditions, J. Solid State Electrochem. 25 (2021) 45–56, https://doi.org/10.1007/s10008-019-04436-w.
[102] W. Zhong, Z. Wang, S. Han, L. Deng, J. Yu, Y. Lin, X. Long, M. Gu, S. Yang, Identifying the active sites of a single atom catalyst with pH-universal oxygen reduction reaction activity, Cell Rep. Phys. Sci. 1 (2020), 100115, https://doi.org/10.1016/j.xcrp.2020.100115.
[103] S. Rojas-Carbonell, C. Santoro, A. Serov, P. Atanassov, Transition metal-nitrogen-carbon catalysts for oxygen reduction reaction in neutral electrolyte, Electrochem. Commun. 75 (2017) 38–42, https://doi.org/10.1016/j.elecom.2016.12.011.
[104] D. Singh, J. Tian, K. Mamtani, J. King, J.T. Miller, U.S. Ozkan, A comparison of N-containing carbon nanostructures (CNx) and N-coordinated iron–carbon catalysts (FeNC) for the oxygen reduction reaction in acidic media, J. Catal. 317 (2014) 30–43, https://doi.org/10.1016/j.jcat.2014.05.025.
[105] M. Muhyuddin, N. Zocche, R. Lorenzi, C. Ferrara, F. Poli, F. Soavi, C. Santoro, Valorization of the inedible pistachio shells into nanoscale transition metal and nitrogen codoped carbon-based electrocatalysts for hydrogen evolution reaction and oxygen reduction reaction, Mater Renew Sustain Energy 11 (2022) 131–141, https://doi.org/10.1007/s40243-022-00212-5.
[106] M. Muhyuddin, D. Testa, R. Lorenzi, G.M. Vanacore, F. Poli, F. Soavi, S. Specchia, W. Giurlani, M. Innocenti, L. Rosi, C. Santoro, Iron-based electrocatalysts derived from scrap tires for oxygen reduction reaction: evolution of synthesis-structure-performance relationship in acidic, neutral and alkaline media, Electrochim. Acta 433 (2022), 141254, https://doi.org/10.1016/j.electacta.2022.141254.
[107] C.H. Choi, C. Baldizzone, J.-P. Grote, A.K. Schuppert, F. Jaouen, K.J.J. Mayrhofer, Stability of Fe-N-C catalysts in acidic medium studied by operando spectroscopy, Angew Chem. Int. Ed. Engl. 54 (2015) 12753–12757, https://doi.org/10.1002/anie.201504903.
[108] Q. Ma, H. Jin, J. Zhu, Z. Li, H. Xu, B. Liu, Z. Zhang, J. Ma, S. Mu, Stabilizing Fe–N–C catalysts as model for oxygen reduction reaction, Adv. Sci. 8 (2021), 2102209, https://doi.org/10.1002/advs.202102209.
[109] T.J. Omasta, L. Wang, X. Peng, C.A. Lewis, J.R. Varcoe, W.E. Mustain, Importance

of balancing membrane and electrode water in anion exchange membrane fuel cells, J. Power Sources 375 (2018) 205–213, https://doi.org/10.1016/j.jpowsour.2017.05.006.
[110] W.E. Mustain, Understanding how high-performance anion exchange membrane fuel cells were achieved: component, interfacial, and cell-level factors, Curr. Opin. Electrochem. 12 (2018) 233–239, https://doi.org/10.1016/j.coelec.2018.11.010.
[111] N. Ramaswamy, S. Mukerjee, Alkaline anion-exchange membrane fuel cells: challenges in electrocatalysis and interfacial charge transfer, Chem. Rev. 119 (2019) 11945–11979, https://doi.org/10.1021/acs.chemrev.9b00157.
[112] P. Teppor, R. J¨ager, M. Paalo, A. Adamson, M. H¨armas, O. Volobujeva, J. Aruv¨ali, R. Palm, E. Lust, Peat as a carbon source for non-platinum group metal oxygen electrocatalysts and AEMFC cathodes, Int. J. Hydrogen Energy 47 (2022) 16908–16920, https://doi.org/10.1016/j.ijhydene.2022.03.199.
[113] J. Lilloja, M. Mooste, E. Kibena-P˜oldsepp, A. Sarapuu, B. Zulevi, A. Kikas, H.-M. Piirsoo, A. Tamm, V. Kisand, S. Holdcroft, A. Serov, K. Tammeveski, Mesoporous iron-nitrogen co-doped carbon material as cathode catalyst for the anion exchange membrane fuel cell, J. Power Sources Adv. 8 (2021), 100052, https://doi.org/10.1016/j.powera.2021.100052.
[114] M. Hao, R. Dun, Y. Su, L. He, F. Ning, X. Zhou, W. Li, In situ self-doped biomass-derived porous carbon as an excellent oxygen reduction electrocatalyst for fuel cells and metal–air batteries, J. Mater. Chem. A. 9 (2021) 14331–14343, https://doi.org/10.1039/D1TA01417J.
[115] L. Wang, M. Bellini, H.A. Miller, J.R. Varcoe, A high conductivity ultrathin anion-exchange membrane with 500+ h alkali stability for use in alkaline membrane fuel cells that can achieve 2 W cm
[116] P.G. Santori, F.D. Speck, S. Cherevko, H.A. Firouzjaie, X. Peng, W.E. Mustain, F. Jaouen, High performance FeNC and Mn-oxide/FeNC layers for AEMFC cathodes, J. Electrochem. Soc. 167 (2020), 134505, https://doi.org/10.1149/1945-7111/abb7e0.
[117] H. Adabi, A. Shakouri, N. Ul Hassan, J.R. Varcoe, B. Zulevi, A. Serov, J. R. Regalbuto, W.E. Mustain, High-performing commercial Fe–N–C cathode

electrocatalyst for anion-exchange membrane fuel cells, Nat. Energy 6 (2021) 834–843, https://doi.org/10.1038/s41560-021-00878-7.

[118] MdM. Hossen, MdS. Hasan, MdR.I. Sardar, J. bin Haider, Mottakin, K. Tammeveski, P. Atanassov, State-of-the-art and developmental trends in platinum group metal-free cathode catalyst for anion exchange membrane fuel cell (AEMFC), Appl. Catal. B: Environ. (2022), 121733, https://doi.org/10.1016/j.apcatb.2022.121733.

[119] X. Peng, V. Kashyap, B. Ng, S. Kurungot, L. Wang, J.R. Varcoe, W.E. Mustain, High-Performing PGM-free AEMFC cathodes from carbon-supported cobalt ferrite nanoparticles, Catalysts 9 (2019) 264, https://doi.org/10.3390/catal9030264.

[120] H. Adabi, P.G. Santori, A. Shakouri, X. Peng, K. Yassin, I.G. Rasin, S. Brandon, D. R. Dekel, N.U. Hassan, M.-T. Sougrati, A. Zitolo, J.R. Varcoe, J.R. Regalbuto, F. Jaouen, W.E. Mustain, Understanding how single-atom site density drives the performance and durability of PGM-free Fe–N–C cathodes in anion exchange membrane fuel cells, Mater. Today Adv. 12 (2021), 100179, https://doi.org/10.1016/j.mtadv.2021.100179.

[121] J. Woo, S.Y. Yang, Y.J. Sa, W.-Y. Choi, M.-H. Lee, H.-W. Lee, T.J. Shin, T.-Y. Kim, S.H. Joo, Promoting oxygen reduction reaction activity of Fe–N/C electrocatalysts by silica-coating-mediated synthesis for anion-exchange membrane fuel cells, Chem. Mater. 30 (2018) 6684–6701, https://doi.org/10.1021/acs.chemmater.8b02117.

[122] Y. Yang, X. Xu, P. Sun, H. Xu, L. Yang, X. Zeng, Y. Huang, S. Wang, D. Cao, AgNPs@Fe-N-C oxygen reduction catalysts for anion exchange membrane fuel

cells, Nano Energy 100 (2022), 107466, https://doi.org/10.1016/j.
nanoen.2022.107466.
[123] W. Xu, D. Yoon, Y. Yang, Y. Xiong, H. Li, R. Zeng, D.A. Muller, H.D. Abruña, MOF-derived bimetallic Pd–Co alkaline ORR electrocatalysts, ACS Appl. Mater. Interfaces 14 (2022) 44735–44744, https://doi.org/10.1021/acsami.2c10074.
[124] S. Das, S. Ghosh, T. Kuila, N.C. Murmu, A. Kundu, Biomass-derived advanced carbon-based electrocatalysts for oxygen reduction reaction, Biomass 2 (2022) 155–177, https://doi.org/10.3390/biomass2030010.